ISTANBUL TECHNICAL UNIVERSITY ★ GRADUATE SCHOOL

RANGE PROFILE EXTRACTION IN NOISE RADARS BASED ON THE TARGET CHARACTERISTICS

M.Sc. THESIS

Şevval KARABAĞ ÇAHA

Department of Electronics and Communication Engineering

Telecommunication Engineering Programme

JANUARY, 2023

ISTANBUL TECHNICAL UNIVERSITY ★ GRADUATE SCHOOL

RANGE PROFILE EXTRACTION
IN NOISE RADARS
BASED ON THE TARGET CHARACTERISTICS

M.Sc. THESIS

Şevval KARABAĞ ÇAHA
(504191338)

Department of Electronics and Communication Engineering

Telecommunication Engineering Programme

Thesis Advisor: Prof. Dr. Selçuk PAKER

JANUARY, 2023

İSTANBUL TEKNİK ÜNİVERSİTESİ ★ LİSANSÜSTÜ EĞİTİM ENSTİTÜSÜ

GÜRÜLTÜ RADARLARINDA HEDEF KARAKTERİSTİKLERİNE DAYALI MENZİL PROFİLİ ÇIKARIMI

YÜKSEK LİSANS TEZİ

Şevval KARABAĞ ÇAHA
(504191338)

Elektronik ve Haberleşme Mühendisliği Anabilim Dalı

Telekomünikasyon Mühendisliği Programı

Tez Danışmanı: Prof. Dr. Selçuk PAKER

OCAK, 2023

Şevval KARABAĞ ÇAHA, a M.Sc. student of ITU Graduate School student ID 504191338, successfully defended the thesis entitled "RANGE PROFILE EXTRACTION IN NOISE RADARS BASED ON THE TARGET CHARACTERISTICS", which he prepared after fulfilling the requirements specified in the associated legislations, before the jury whose signatures are below.

Thesis Advisor :	**Prof. Dr. Selçuk PAKER** Istanbul Technical University	....
Jury Members :	**Prof. Dr. Mesut KARTAL** Istanbul Technical University	....
	Dr. Serdar KARGIN Istanbul Arel University	....

Date of Submission : 21 October 2022
Date of Defense : 6 January 2023

To my family...

FOREWORD

Firstly, I would like to thank my advisor Prof. Dr. Selçuk Paker for his support and guidance throughout my graduate studies. I appreciate his guidance, support, and creative suggestions throughout my research. I am truly thankful for his patience and encouragement to finish my work.

I would like to thank TUBITAK for financial support.

I would also like to thank my beloved family. I could not achieve anything without my father, mother, and sisters. I am very grateful to my dearest family for their endless patience and unconditional love.

At last but at the most, I would like to thank my dearest Taylan Çaha for his great love, patience, guidance, and support during my life and this study.

January, 2023 Şevval KARABAĞ ÇAHA

TABLE OF CONTENTS

Page

ABBREVIATIONS

ADC	: Analog to digital converter
AoA	: Angle-of-Arrival
BLASA	: Band limited algorithm for side-lobes attenuation
DAC	: Digital analog converters
ECCM	: Electronic counter countermeasure
FFT	: Fast Fourier transform
FMCW	: Frequency-modulated continuous-wave
FPGA	: Field programmable gate arrays
GO	: Geometric optics
IF	: Intermediate frequency
LFM	: Linear frequency modulated
LNA	: Low noise amplifier
LO	: Local oscillator
MLS	: Maximum length sequences
PDF	: Probability density function
PRF	: Pulse repetition frequency
PPI	: Plan position indicator
PRN	: Pseudo-random noise
PN	: Pseudo noise
PRI	: Pulse repetition interval
RCS	: Radar cross dection
RSR	: Random signal radar
RF	: Radio frequency
SAR	: Synthetic aperture radar
SNR	: Signal-to-noise ratio
UWB	: Ultra wide band
VCO	: Voltage control oscillator

SYMBOLS

τ_t	: Pulse width
T_{PRI}	: Pulse repetition interval
c	: Speed of light
R_T	: Target range
P_a	: Average transmitted power
P_t	: Transmitted power
R_{max}	: Maximum ambigitious range
ΔR	: Range resolution
B	: Bandwidth
P_R	: Received power
G_T	: Transmit antenna gain
G_R	: Receive antenna gain
σ	: Radar cross section
L	: Losses
λ	: Wavelength
A_σ	: Target reflectivity
$\lvert . \rvert$	: Absolute value
$(.)^*$	: Complex conjugate of matrix
θ_k	: Phase parameter
N	: Code length
$\exp(.)$	: Exponential function
$\oplus$	: Modulo 2 addition operation
τ_{chip}	: Chipwidth
V	: Voltage
I	: Current
f_s	: Sampling rate
T_s	: Sampling interval
E_i	: Transmitted electric field
E_s	: Back-scattered electric field
dS	: Surface patch
ψ	: Green function
$J_1(.)$	: First order Bessel function

LIST OF TABLES

Page

LIST OF FIGURES

Page

RANGE PROFILE EXTRACTION
IN NOISE RADARS
BASED ON THE TARGET CHARACTERISTICS

SUMMARY

Continuous and pulsed radar systems are frequently used in military and civilian applications. The detection capability of a radar depends on the antenna properties used, the size and material properties of the target to be detected, the noise level of the receiving antenna and the RF line, and the effective output power of the radar, which is one of the most important. The effective output power of radar systems increases in direct proportion to the pulse width, thus improving the signal-to-noise ratio (SNR). A high SNR level improves detection performance and measurement accuracy. However, in conventional pulse radar, increasing the pulse length causes a decrease in the range resolution, which is undesirable. Different types of pulse compression are used to achieve high output power and low range resolution. These include frequency modulation and phase modulation. One of the most popular frequency modulations is the pulse compression technique based on linear frequency modulation. In phase modulation, which is another method, the phase of the radar pulse can be generated by different intrapulse modulations such as binary phase modulation, poly-phase modulation, and noise or pseudo-noise modulations. Phase-modulated waveforms are obtained by dividing a pulse into multiple sub-pulses to achieve the required main lobe and side lobe levels. The length of a single sub-pulse obtained defines the radar's range resolution. Bi-phase encoded waveforms exhibit two possible phase states, typically 0 and 180 degrees, while poly-phase codes exhibit more than two phase states.

In this study, phase modulation of the radar is provided with binary phase-coded pseudo-random noise. Noise form is used because of the advantages it adds to the radar. The first advantage of noise waveforms over deterministic classical radars is that there is no uncertainty in the radar's range and velocity resolution. Since the waveforms produced by the radar are independent of each other, there is no ambiguity between the two pulses when interpreting the incoming echo signals. Another advantage is that it is less likely to be affected by other signal sources in the environment, thanks to the waves it creates in different forms. Therefore, there is no interference problem with other antennas broadcasting on the same platform. In military applications, it is a form of radar that is resistant to electronic warfare systems. Because radars using the noise radar form are difficult to find in threat libraries. At the same time, even if detected, it is close to impossible to apply other phase-matched techniques except noise mixing techniques.

Within the scope of the study, a digital pseudo-noise dual phase coded radar design was carried out. With this design, the signal in the intermediate frequency or base-band generated by the digital card is increased to high frequencies with the help of the

upper band frequency converter. Then, with the help of a power amplifier and antenna, radar broadcasts towards the target object. The echo signal scattered from the target is received again with the help of the antenna. Then, the range and size information of the target is obtained. The echo signal from the radar is first amplified with the help of the circuit located behind the antenna. In this way, the required sensitivity is achieved without reducing the signal strength before it enters the receiver. Then, with the help of a pre-filtering circuit, the signal from different frequency bands is prevented from entering the receiver circuit. The radar signal coming at high frequency is first reduced to the higher frequency bands by two local oscillators and then to a sampling frequency where the ADC is suitable. The reason for using two different local oscillators is to get rid of radar interference and image signals. As a result, the radar echo brought into digital form is ready for signal processing algorithms.

With the help of correlation applied in the signal processing block, the range and size information of the target is tried to be extracted. In this study, a rectangular prism was used as the target object and it is divided into equal and small triangular parts. The process continued, assuming that the prism is a perfect electrical conductor. The radar cross-sectional area of the triangles, which are each small sub-unit, was calculated by physical optics methods and the reflection intensity was calculated according to the angle it made with the radar platform.

The radar platform is designed as a drone's payload. The target object was illuminated by making different flight profiles from a close area of approximately 200 - 300 meters. In the MATLAB program, the range and size information of the target was extracted using signal processing algorithms based on the correlation method.

GÜRÜLTÜ RADARLARINDA HEDEF KARAKTERİSTİKLERİNE DAYALI MENZİL PROFİLİ ÇIKARIMI

ÖZET

Sürekli ve darbeli radar sistemleri askeri ve sivil uygulamalarda sıkça kullanılmaktadır. Bir radarın tespit edebilme yeteneği, kullanılan anten özelliklerine, tespit edilmek istenen hedefin boyutu ve materyal özelliklerine, alıcı anten ve RF hattaki gürültü seviyesine ve en önemli parametrelerden olan radarın efektif çıkış gücüne bağlıdır. Radar sistemlerinin etkin çıkış gücü darbe genişliğiyle doğru orantılı olarak artar, böylece sinyal-gürültü oranında (SNR) iyileşme görülür. SNR seviyesinin yüksek olması algılama performansını ve ölçüm doğruluğunu iyileştirir. Ancak klasik bir darbe radarında darbe uzunluğunu artırmak istenmeyen bir durum olarak menzil çözünürlüğünün azalmasına sebep olur. Yüksek çıkış gücü ve düşük menzil çözünürlüğü elde edebilmek için farklı darbe sıkıştırma türleri kullanılır. Bunlar arasında frekans modulasyonu ve faz modulasyonu vardır.

Frekans modulasyonları arasında en popüler olanı lineer frekans modülasyonuna dayalı darbe sıkıştırma tekniğidir. Diğer bir yöntem olan faz modülasyonunda ise ikili faz modülasyonu, çok fazlı modülasyon ve gürültü veya sözde gürültü modülasyonları gibi farklı darbe içi modülasyonlarla radar darbesinin fazı üretilebilir. Faz modülasyonlu dalga formları, gereksinim duyulan ana lob ve yan lob seviyelerini elde edebilmek için bir darbenin birden fazla alt darbeye bölünmesiyle elde edilir. Elde edilen tek bir alt darbenin uzunluğu, radarın menzil çözünürlüğünü tanımlar. İki fazlı kodlu dalga biçimleri, tipik olarak 0 ve 180 derece olmak üzere iki olası faz durumu sergilerken, çok fazlı kodlar ikiden fazla faz durumu sergiler.

Bu çalışmada ikili faz kodlu sözde rastgele gürültü ile radarın faz modülasyonu sağlanmıştır. Deterministik klasik radarlara kıyasla gürültü dalga biçimlerinin ilk avantajı radarın menzil ve hız çözünürlüğünde belirsizlik oluşmamasıdır. Radarın ürettiği dalga formları birbirinden bağımsız olduğu için gelen yankı sinyalleri anlamdırılırken iki darbe arası belirsizlik oluşmaz. Bir diğer avantajı ise farklı formda oluşturduğu dalgalar sayesinde ortamda bulunan diğer sinyal kaynaklarından etkilenme olasılığının düşük olmasıdır. Bu nedenle, aynı platformda bulunan ve yayın yapan diğer antenlerle interferans sorunu yaşanmaz. Askeri uygulamalarda ise elektronik harp sistemlerine karşı dayanıklı bir radar formudur. Çünkü, gürültü radar formu kullanan radarlar tehdit kütüphanelerinde bulunması zor radarlardır. Aynı zamanda, tespit edilse dahi gürültü karıştırma teknikleri haricinde diğer evre uyumlu teknikleri uygulamak imkansıza yakındır.

Çalışma kapsamında dijital sözde gürültü ikili faz kodlu radar tasarımı gerçekleştirilmiştir. Bu tasarım ile esas olarak sayısal kart tarafından üretilen orta frekans ya da

temel bantta bulunan sinyal, üst bant frekans çevirici yardımıyla yüksek frekanslara çıkarılır. Sonrasında, güç yükselteç ve anten yardımıyle hedef cisime doğru yayın yapılır. Hedeften saçılan yankı sinyali tekrar anten yardımıyla alınir ve hedefin menzil, boyut bilgileri elde edilir. Radardan gelen yankı sinyali ilk olarak anten arkasında bulunan önkat devresi yardımıyla düşük olan gücü yükseltilir. Bu sayede, alma hattına girmeden önce sinyal gücü düşmeden gerekli duyarlılık sağlanır. Daha sonra, bir ön filtreleme devresi yardımıyla, farklı frekans bantlarından gelen sinyalin alıcı devreye girmesi engellenir. Yüksek frekansta gelen radar sinyali iki adet lokal osilatör tarafından önce daha yüksek frekans bantlarına daha sonra analogtan sayısala dönüştüren çeviricilerin uygun olduğu bir örnekleme frekansına indirilir. İki farklı lokal osilatör kullanımının sebebi radar parazit ve imaj sinyallerinden kurtulmaktır. Sonuç olarak, sayısal forma getirilen radar yankısı, sinyal işleme algoritmaları için hazır hale getirilmiş olur.

Sinyal işleme bloğunda uygulanan korelasyon yardımıyla, hedefin menzil ve boyut bilgisi çıkarılmaya çalışılır. Bu çalışma kapsamında, hedef cisim olarak eşit ve küçük üçgen parçalarına ayrılmış dikdörtgenler prizması kullanılmıştır. Prizmanın perfect elektrik iletken olduğu kabul edilerek işlemlere devam edilmiştir. Her bir küçük alt birim olan üçgenlerin radar kesit alanı fizik optik yöntemleri ile hesaplanmıştır ve radar platformu ile yaptığı açıya göre yansıma şiddeti hesaplanmıştır.

Tasarımı yapılan radar sistemi başlangıçta noktasal saçıcılar için denenmiştir. 4 adet saçıcı nokta uzayda yerleştirilmiş ve radar göre konumları çıkarılmıştır. Nokta konumları başarılı bir şekilde tespit edilebilmiştir. Radar faz kodunda kullanılan sözde rastgele dizisi 1024 uzunlukta seçilmiştir. Daha sonrasında karşılaştırma yapabilmek adına uzunluğu 16'dan başlayarak 512'ye kadar olan dizi uzunlukları ile nokta saçıcıların konumu belirlenmeye çalışılmıştır. Daha kısa olan 16 uzunluklu dizi ile oluşturulan faz kodlu radarın performansının kötü olduğu kanısına varılmıştır.

Devamında ise radar sistemi, döner kanat bir insansız hava aracının faydalı yükü olarak geliştirilmiştir. Bu sayede farklı uçuş profilleri oluşturulabilmiş ve ve simülasyon sonuçları detaylandırılabilmiştir. Hedef cisimden yaklaşık 100 metre kadar irtifada uçurulması tercih edilmiştir. Hedef cisim olarak dikdörtgenler prizması kullanılmıştır. Bu şekilde bir yapının kullanılmasının sebebi binaya benzer yapılar simüle edebilmek olmuştur.

Çalışmanın başlangıcında tek bir prizma kullanılmıştır ve her bir kenarı küçük üçgenlere Kullanılan cisim 40 metre genişliğinde olup, 5 metre yükseklikte ve derinlikte seçilmiştir. Radar platformu lineer uçuş yaparak 64 ayrı lokasyondan bilgi toplamıştır. Rastgele seçilen iki noktadan gelen verilerle cismin menzil profili çıkarılmıştır. Çıkan sonuçlar doğrultusunda hedefin radardan uzaklığı ve yaklaşık boyutları konusunda bilgi elde edilebilmiştir. Radarın yaptığı lineer uçuş dolayısıyla B tarama yapılmıştır. Radarın düz uçuşunda topladığı her bir menzil profili bir araya getirildiğinde beklendiği üzere hiperbolik bir görüntü oluşmuştur. Bu B tarama görselinin çıkarabilmek için oluşan hiperbolik görüntü çeşitli algoritmalar yardımıyla odaklanılmış ve cizmin tarama görüntüsü elde edilmiştir.

Daha sonrasında aynı uçuş için 2 hedef cisim konumlandırılmıştır. Bu iki cisim eş iki cisim olarak seçilmiştir. 20 metre genişliğinde 10 metre yükseklikte ve 5 metre derinliğinde olan bu iki cisim birbirlerini gölgeleyemeyecek şekilde yerleştirilmiştir. Aynı işlemler tekrarlandığında iki cismin birbirinden ayırt edilebildiği ve aynı şekilde menzil profillerinin başarıyla elde edildiği gözlemlenmiştir.

Radarın bulunduğu platform çember şeklinde bir uçuş yaptırılarak 64 ayrı noktadan sonuçlar toplanmıştır. Bunun amacı cismin tüm açılardan menzil bilgisini çıkarmak olmuştur. Radarın farklı lokasyonlarından elde edilen menzil profilleri yardımıyla cismin boyutları hakkında yorum yapılabilir hale gelmiştir. Her bir menzil profilinden elde edilen cisim boyutları çıkarılarak tüm yanca açılarında karşılaştırılmıştır. Bunun sonucunda simetrik bir grafik elde edilmiştir. Bu karşılaştırmayı daha sağlıklı yapabilmek amacıyla iki ayrı cisim için simülasyon sonuçları toplanmıştır. Kullanılan ilk cisim 40 metre genişliğinde ve 5'er metre yükseliğind eve genişliğindedir. Diğer cisim boyutları ise 20 metre genişliğinde, 10 metere yükselikte ve 5 metre derinlikte olacak şekilde belirlenmiştir. Bu iki cismin her bir yanca açısı için boyut bilgileri olan simetri grafikleri çıkarılmıştır ve son olarak da 64 farklı noktadaki menzil profili görüntüleri çıkarılmıştır.

1. INTRODUCTION

A radar is an electromagnetic-based system used to determine the distance and position of an object from its location. Radar systems basically work by spreading the energy carried by the electromagnetic signal and detecting the echo, that is, the echo signal, returning from the targets where this electromagnetic energy is reflected. The structure of the echo signal includes data about the target, including the distance of the radar to the target and the speed of the target. Radar systems can also be classified as continuous waveform radar and pulse radar according to the characteristics of the signals transmitted by the transmitter. Continuous waveform radar transmits a single continuous waveform, while pulse radar transmits very short pulses. This information about the target is detected by applying signal processing algorithms to the waveform of the echo received by the radar system [5]. Continuous wave radars continuously emit a high-frequency sinusoidal signal. Unmodulated continuous wave radars can accurately measure the speed of the target by Doppler shift. But in such radars, range information cannot be obtained without using a modulation technique. Unmodulated continuous wave radars are mainly used for the purpose of obtaining velocity information of the target and tracking the target. In order to obtain the distance information of the target, the carrier frequency must be modulated. Noise radar technology has formed a good stepping stone in developing modern radar systems. The main feature of noise radars is that they use random or pseudo-random waveforms. These systems have a wide range of uses such as surveillance, tracking, tracking, and collision warning radars. Deterministic waveform radars use low pulse length waveforms with very high peak power to achieve long-range detection capability. The transmitted pulse width can be changed by setting the maximum output power. However, increasing the pulse width with conventional radar causes the range resolution to deteriorate, which is an undesirable situation. A low output power reduces the performance of the radar, so pulse compression techniques can be used to solve this problem. The most popular among them is compression based on linear frequency modulation. Different intrapulse modulation techniques, including binary-phase modulation, polyphase modulation, noise or pseudo-noise modulation, have been researched to enhance the characteristics of the radar [4].

1.1 Aim of Thesis

In this study, the payload of the drone, which is an unmanned aerial vehicle, is designed to be a radar, and a pseudo-noise phase-coded radar design is recommended in order to determine the range and size of the targets in the close area of about 200 meters away. In order to obtain realistic results by creating this target object with the help of a simulation program, a range and size estimation is made by calculating the radar cross-sectional areas of each divided into small pieces. Reflections from each small unit are processed by a signal with the help of correlation. In this way, the intensity and range of the reflections from the object can be easily detected.

1.2 Literature Review

In 1959, noise radars were developed for the first time to measure distance. To begin with, analog circuit components were used in the creation of the radar [6]. In the late 1990s, coherent ultra-wideband (UWB) random noise systems for Doppler estimation [7, 8] and aerial imaging [9] were designed using noise radar technology, and range side lobe suppression of a novel UWB random noise radar approach was suggested and investigated. Noise radar has been in development at the Laboratory of Nonlinear Dynamics of Electronic Systems of IRE NASU since 1993. To prove the usability of noise radar for the design of different radar systems and the prediction of their critical performance metrics, a variety of prototypes and functional noise radars have been built. In 2008, for example, the world's first pulse coherent surveillance noise radar was developed, made, and delivered to a customer. With the help of synthetic aperture radar (SAR), an image of the ground is created with a simple method. There is no theoretical connection between SAR and noise radars, but it has been demonstrated by

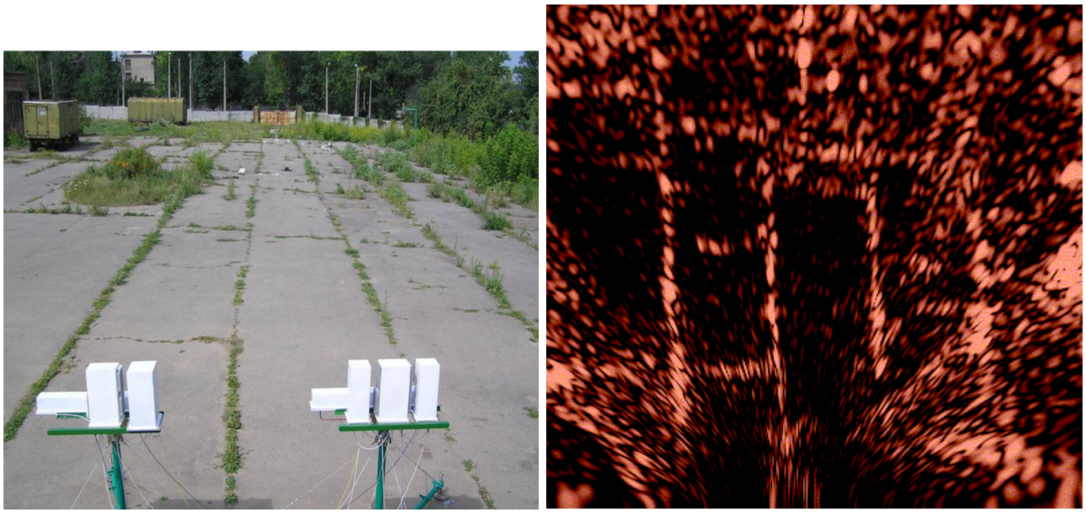

(a) Optic image (b) Radar image

Figure 1.1 : Images of an abandoned basketball court [1].

the study here that images can be easily obtained with random waveforms. Because of qualities like interference immunity, the ability to generate a signal with Gaussian spectra with a low side-lobe level, and the unpredictability of the pulses, which allows for a greater pulse repetition frequency (PRF) than deterministic signals, airborne and space-borne SAR can benefit from utilizing the noise radar [10].

In 2008, with the help of the first NATO group on noise radar, a sequence of demonstrations utilizing this radar were performed in Kharkiv, Ukraine. The testing resulted in a picture of a lake with houses detected at a distance of roughly a kilometer, which was an early indication that noise radar could be utilized at realistic ranges outside of the lab. Fig. 1.1 is a SAR radar picture of a decommissioned basketball court. This demonstrates the excellent sensitivity and resolution with which the gaps between the asphalt slabs can be seen [11]. In another study, noise radars were used for behind-the-wall imaging. The short-pulse waveforms used by standard through-wall imaging technologies are plainly observable and may be blocked with the right countermeasure techniques. This kind of imaging might give false results as a result of jamming and notifies the occupants that they are being examined. Due to its low probability of intercept and low probability of detection, noise radar performs better in this application. As a result, noise radar systems are an excellent choice for inside

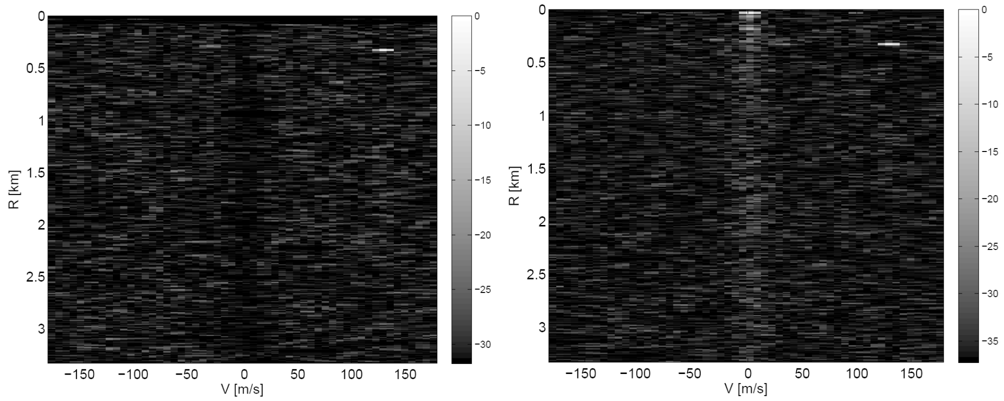

(a) Calculated correlation function for impulsive noise-filled received signal.

(b) The received signal's correlation function following the robustification process.

Figure 1.2 : Correlation function for before and after robustification process [2].

imaging systems [12]. Additionally, target detection with continuous noise wave radars was studied. Random or pseudo-random waveforms are preferred as noise. Target detection was attempted by using classical correlation receivers. The effectiveness of the detection decreases if the external noise has a non-Gaussian distribution, such as impulsive noise. A robustification technique is suggested in order to recover the sensitivity that was lost as a result of the impulsive noise. The approach involves applying a nonlinear function to the signal in order to filter out the outliers. Real-world signals are used to validate the approach. While Fig. 1.2(a) shows the absolute value of the correlation value, Fig. 1.2(b) shows the state after the robustification process. In the study, a method has been proposed to improve the detection capability of the radar. The method was previously tested in the simulation environment and then applied to real-time signals. This method has also been shown to be quite successful in real-time signals. In the last case, there was a $5dB$ improvement in the signal-to-noise ratio (SNR) of the signal [2]. At the Turkish Naval Research Center Command (TNRCC) test site outside Istanbul, Turkey, the NATO SET-225 "Spatial and Waveform Diverse Noise Radar" researchers performed shore-based maritime experiments in December 2018 [3]. This study presents the preliminary results of experiments with a noise radar demonstrator, which has an antenna design resembling a compact conventional maritime radar and a noise-limited sensitivity. This study is the first trial of a noise radar display with antenna configuration and operating with

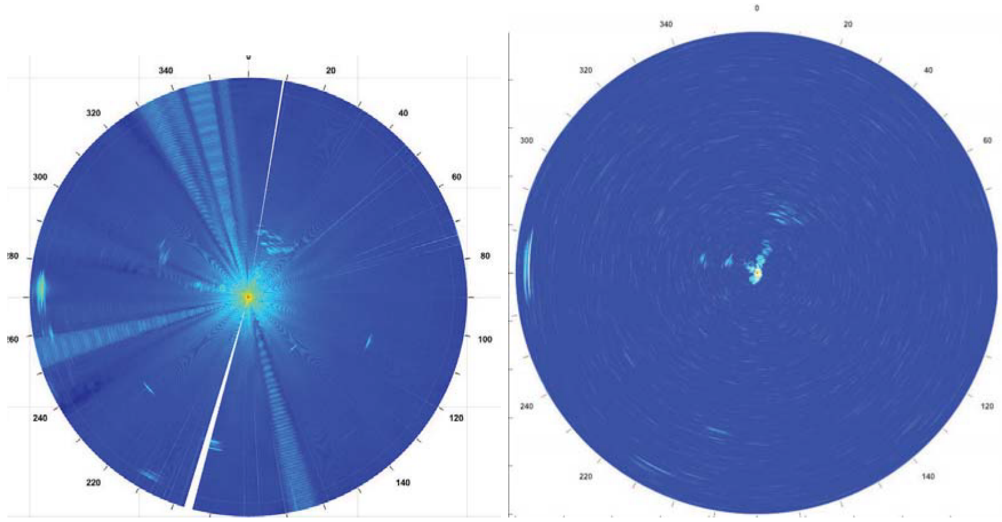

(a) LFM radar PPI scope (b) Noise radar PPI scope

Figure 1.3 : PPI displays for comparison of two radars [3]

noise signals similar to a relatively small conventional marine radar currently in use. This deterministic marine radar uses a linear frequency modulated (LFM) waveform. The decisive factor of this work is to obtain a plan position indicator (PPI) screen. One of the important and decisive subjects was dynamic field control. In order to expand the useful dynamic range of these studies and to find effective results, Band Limited Algorithm for Side-lobes Attenuation (BLASA) algorithm applied slash forms were used. The details of BLASA are also explained in this study. The PPI display of a normal and deterministic radar and noise radar up to $3\,km$ is given in Fig.1.3. Targets are shown in red circles on the PPI screen of both radars. While the sensitivity of the noise radar in Fig.1.3(a) is worse than the LFM case shown in Fig.1.3(b), it is less affected by the interference noise around the same frequency. The PPI displays that the radar has successfully produced would be appropriate for small boats to use for naval orientation. The benefits of customized BLASA waveforms in lowering the range side-lobe level to increase the radar's usable sensitivity have also been shown [3].

1.3 Contribution

There are many studies on noise radars in the literature. The use of noise radars in the world has increased in the areas of target detection, target tracking and radar imaging.

In this study, noise radars are used in phase modulation of numerically coded radars. With the pseudo noise code used in different code lengths, the ranges of point scatterers and different targets are extracted. Unlike other studies, the radar target is created in the MATLAB environment and divided into small pieces and the radar cross-sectional area of each is calculated. Thus, more realistic results are obtained. At the same time, the drone, which is an unmanned aerial vehicle whose use of radar platform is becoming more and more widespread in the world, is selected and by moving it in different flight profiles, radar echo signals are collected and information about the position and size of the object is obtained.

2. PRELIMINARIES OF RADAR SYSTEMS

In this section, some essential radar signal processing theory is presented for background motivation. In Section 2.1, some radar basics, and waveform expressions are described. Section 2.2 discusses the noise radar fundamentals. Finally, phase compression and code sequences which include Barker codes, Frank codes, P1, P2, and Px codes, Zadoff-Chu code, and pseudo-noise code sequences are explained in Section 2.3.

2.1 Radar Basics

Radar is the abbreviation of Radio Detection And Ranging. It is mainly used to determine, detect or track some target objects by extracting their range and closing velocity information. Additionally, radars are able to detect the angle-of-arrival (AoA) of the returning radar signals. The radar is based on transmitting an electromagnetic wave from the antenna towards a scene and receiving the echo signal. After some receiver operations, the detections and measurements are made. The time delay of the signal is connected to the range of the targets. The range is calculated as half of the delay multiplied by the speed of propagation because of the round trip of the echo signal.

In radar systems, range resolution can be considerably improved by using very short pulses. However, the average transmission power decreases with the use of short pulses, and this can lead to results that may interfere with the normal operating mode of the radar. The average transmit power is directly related to the signal-to-noise ratio (SNR) of the receiver, and the SNR can be increased by increasing the pulse width. SNR, which is a function of the energy in the pulses generated in radar systems, is a measure of the radar's performance in detecting targets and the measurement accuracy of the distance to the target [13, 14].

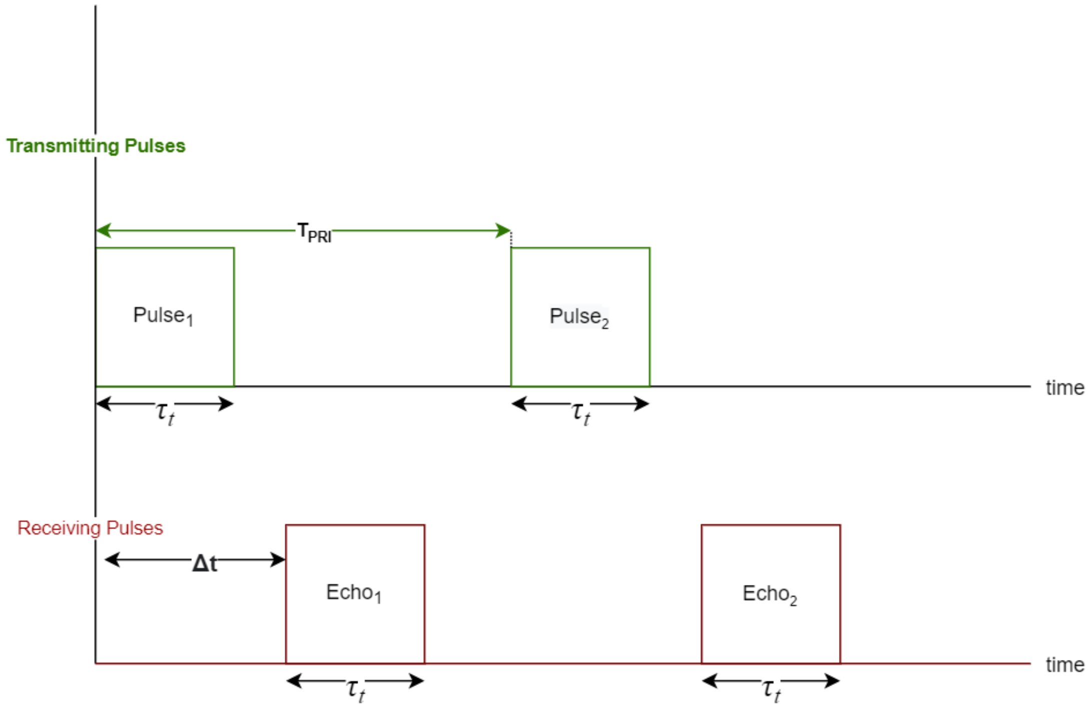

Figure 2.1 : Transmitting and receiving time windows.

Frequency and phase-modulated waveforms are used in modern radar systems. Needs and limits such as bandwidth, sampling rate, power, side lobe, SNR, and range resolution characteristics are taken into account while creating the waveform. Many waveform modulation approaches for both continuous wave and pulsed radars have been developed to satisfy all of these criteria of the radar system. The bandwidth of the waveform may be extended by using modulation methods in the radar, resulting in a higher range resolution for the waveform without affecting the pulse width.

Modern radar sensors generally use a linear frequency-modulated continuous-wave radar signal as the transmission signal. Benefiting from the increasing capabilities of digital circuits, which are widely used today, becomes attractive in many areas, as well as in the development of radar systems used in autonomous systems and the automotive field [15]. Phase-coded radars can be preferred due to the ease of working with digital circuits, and the simulation of digital phase-coded radars will be explained in the continuation of this study. Firstly, pulse radars need to be mentioned to understand phase-coded radars. Radar systems that use pulsed waveform as radar signals send a modulated pulses array with pulse width τ_t and wait for pulsed signals reflected from the target between the transmitted pulses. This pulsed waveform envelope contains the carrier.

As can be seen in Fig. 2.1, the time interval between two consecutive pulses is known as the pulse repetition interval (PRI) that is denoted T_{PRI}. The inverse of PRI is pulse repetition frequency (PRF). PRF is the rate during which pulses repeat per second and it is defined as

$$\mathrm{PRF} = \frac{1}{T_{\mathrm{PRI}}}. \tag{2.1}$$

Range to the target calculated as

$$R_T = \frac{c \times \Delta t}{2}, \tag{2.2}$$

where bidirectional time delay between a transmitted and received pulse is defined with Δ_t and c is speed of light [5]. Radar systems are designed to collect echoes within a specific range window with start and endpoints. The receiver of the radar system is activated at a time delay corresponding to the starting point and deactivated at a time delay corresponding to the completion of the collection range of echoes containing the endpoint. The time delay is defined as

$$\Delta t = \frac{2R_T}{c}. \tag{2.3}$$

The received signal in a current radar system is often sampled at discrete time intervals using an analog to digital converter (ADC), which quantizes the signal in both time and amplitude [16].

The period between observations must be less than a pulse width to allow observation. Also, after a pulse is transmitted, the time elapsed until the incoming echo signal gives the distance of the target. If the incoming echo signal is transmitted after the first pulse but comes after the second pulse, it creates an ambiguity in the range. The Pulse_1 rectangles denote transmitted pulses, while the Echo_1 rectangles denote received echoes from two different targets(A and B) as seen in Fig. 2.2. The time delay from the first target A is smaller than T_{PRI}, but the time delay from target B is greater than T_{PRI} and indicated by T_a. Therefore, the echo signal from target B came after the next pulse.

$$R_{\max} \leq \frac{c \cdot T_{\mathrm{PRI}}}{2} \tag{2.4}$$

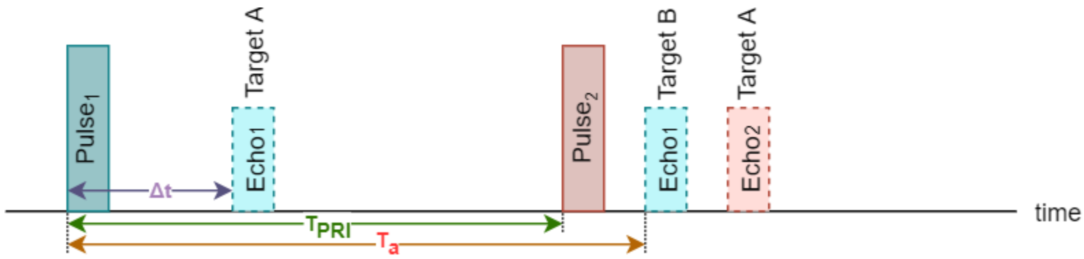

Figure 2.2 : Radar range ambiguity.

As a result, in order to avoid range ambiguities, the (2.4) should be fulfilled. The width of the pulses (τ_t) used as the radar waveform is closely related to the bandwidth (B) of the radar system and determines the range resolution.

Range resolution, on the other hand, is defined as the ability of the radar to distinguish between targets within its range. The quality of range resolution in a radar system depends on the width of the pulse transmitted by the system, the type, and size of the targets in its range. Among them, the most critical factor determining the range resolution is the pulse width parameter. When the radar waveform is not modulated, the range resolution (ΔR) is defined as

$$\Delta R = \frac{c \times \tau_t}{2} = \frac{c}{2B}. \tag{2.5}$$

Fig. 2.3 shows the receiver output for a single transmitted pulse echoed by two-point scatterers. If the ΔR is large enough, the range information can be distinguished in two different ways. However, when the R is not large enough, as seen in Fig. 2.3, overlap may occur and two different range points cannot be distinguished from each other.The waveform used here is an unmodulated waveform. [16].

2.2 Noise Radar Fundamentals

The phrase “noise radar” refers to a collection of radars that illuminate targets with a random or pseudo-random waveform signal. This sort of radar is referred to as a random signal radar (RSR) in numerous publications [1]. This type of radar can be used in a wide range of applications. Random noise signals can be used to build surveillance, tracking, guiding, collision warning, subsurface, and other

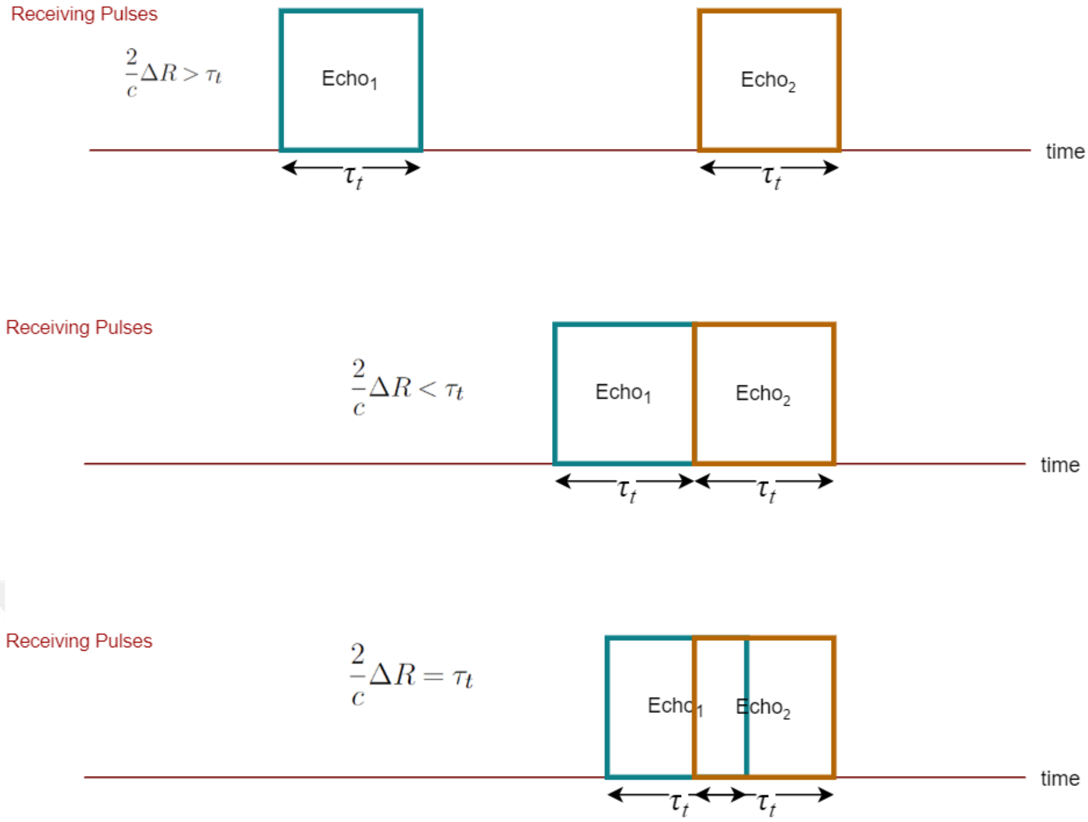

Figure 2.3 : Overlap of pulse window for close target points.

radars. Compared to pulse, pulse-Doppler, and frequency-modulated continuous-wave (FMCW) radars, noise radars have various benefits.

According to the literature, a noise waveform signal provides an absence of range and Doppler ambiguity, low peak power, and exceptionally good electromagnetic compatibility with other systems using the same frequency range. Noise radars offer excellent electronic counter countermeasure (ECCM) capabilities due to their low peak output power. Noise radars are very difficult to detect, identify and classify in electronic warfare systems. Unfortunately, this form of radar has several weaknesses. In comparison to the comparable pulse radar, signal processing in a noise radar is clearly more challenging. The needed computational power is rather large, and performing noisy radar signal processing in real-time for high-bandwidth radars is difficult. Near-far problems, which are well-known in the radio broadcast, also affect noise radars. Because the received electromagnetic power varies with the fourth power of the range, long-range radars require a very large effective dynamic range [1, 4, 12].

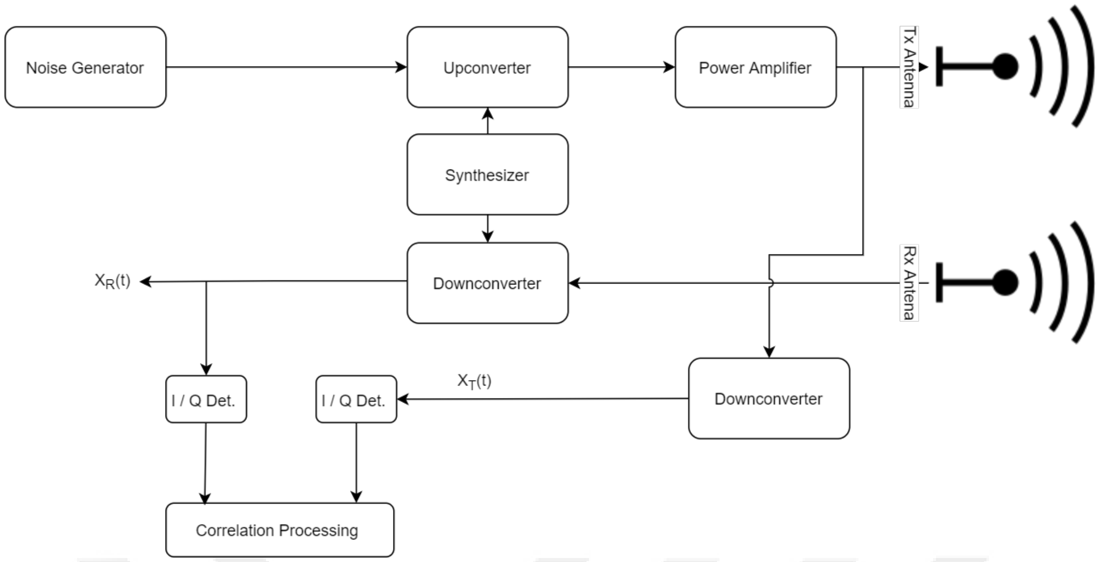

Figure 2.4 : The structure of the noise radar [4].

The target is illuminated with a noise waveform and the echo is listened to by noise radar. In the noise generator, the noise signal is produced. This generator can be made using an analog method, such as amplifying thermal noise, or a digital technique, such as repeating data samples in memory and converting them to an analog signal using fast digital analog converters (DAC).

In general cases, the signal-generating unit produces a signal in a complex form. The band-limited signal generated can be shifted to the base-band to increase the processing capabilities. In essence, a noise signal is produced with the help of a noise generator, as seen in Fig. 2.4. In the up-converter block, the signals produced in the base-band are carried to high frequencies with the help of the mixer. The high-frequency signal passes through the power amplifier and is broadcast by the transmit antenna. With the use of a mixer in the down-converter block, the incoming echo signal is shifted to the base-band frequency. The $x_R(t)$ signal at the output of the down-converter is in complex form, and it is digitized in the correlation block and the signal processing steps are applied here. In the second down-converter used, the transmitting signal is shifted in the base-band, the signal is converted into digital form and enters the correlation processing block. When the signal in the base-band produced by the noise generator reaches a high frequency and is transmitted, hardware distortion may occur. Therefore,

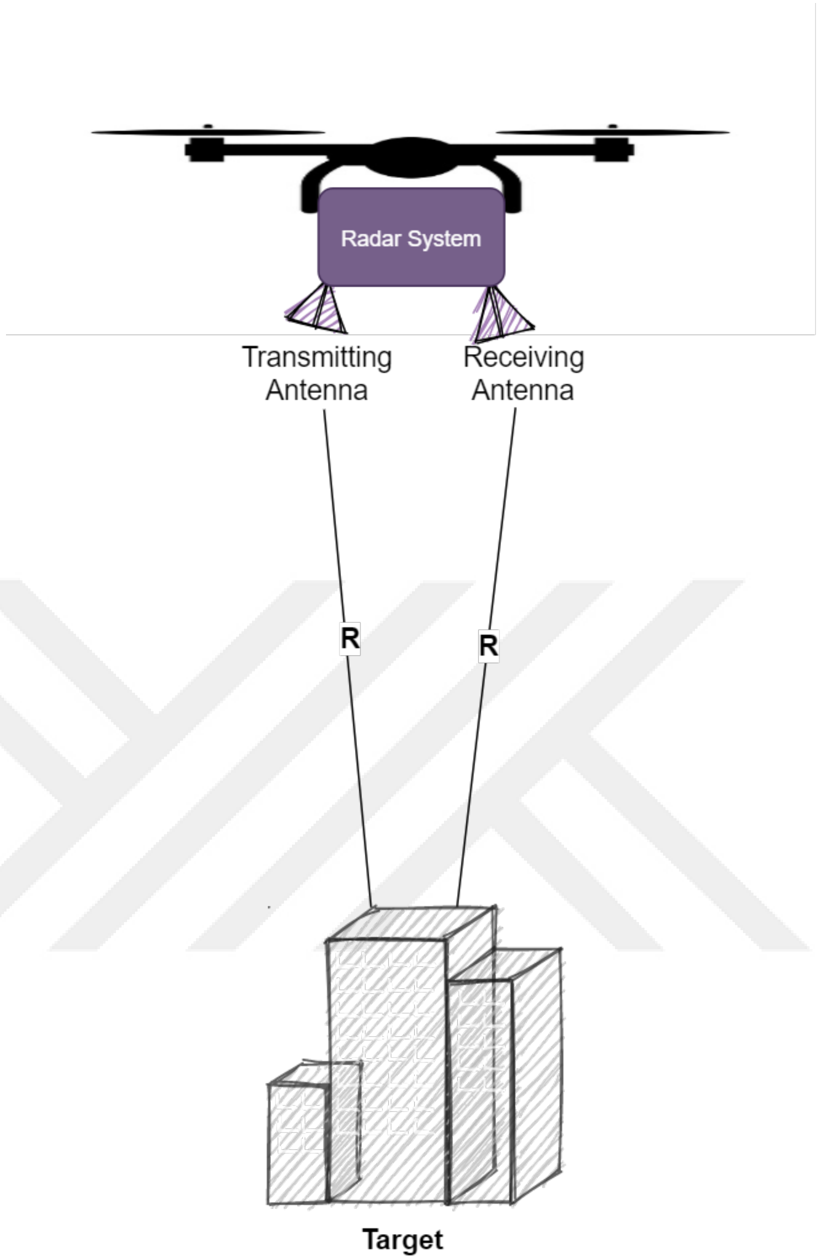

Figure 2.5 : Radar scenario with separate transmit and receive antennas.

the signal in front of the antenna is generated by the second down-converter, which is the reference signal $x_T(t)$ [4]. In Fig. 2.5, the radar system is placed as the payload of the unmanned aerial vehicle with different receiving and transmitting antennas, and the target with R distance is a building [4, 12]. This type of radar uses correlation instead of the matched filter used for normal radar target detection. In the principle of the correlation process, it looks at the relationship between the transmit signal and the time-delayed incoming echo signal. The peak value in this process gives the distance to the target. The expression giving the correlation between the transmit and the received signal is given as

$$R(\tau) = \int_{t=0}^{t_i} x_R(t) x_T^*(t-\tau) dt, \tag{2.6}$$

where the integration time is t_i, $x_T(t)$ is the transmit signal and $x_R(t)$ is the receive signal [12]. The received signal for a single point target in the radar's line of sight is given as

$$x_R(t) = A_\sigma x_T (t - \Delta_t) + n(t), \tag{2.7}$$

where Δ_t represents the time delay of the echo signal. A_σ represents target reflectivity, while $n(t)$ is added to indicate undesired noise [4, 12].

In the noiseless case where $n(t) = 0$, if $\tau = \Delta_t$, it is observed that there is a maximum correlation peak. The time delay created by the r_0 range is calculated with the formula $\Delta_t = 2r_0/c$.

2.3 Phase Compression and Code Sequences

As can be seen from (2.5), decreasing pulse width causes the average transmitted power of the radar to decrease and the operating bandwidth to increase. At this point, pulse compression techniques are used to bring the range resolution to the desired level in order to increase the radar performance while providing sufficient average transmitted power. In radars using the pulse compression method, the range resolution is now related to the width of the pulse transmitted by the radar. It is determined by the width of the pulse that occurs after the pulse compression. In this way, it can be said that these radars have achieved a much better range resolution despite the long pulses transmitted. Pulse radar waveforms are fully defined by taking into account the parameters of pulse repetition frequency, pulse width, and carrier frequency, as well as the modulation technique. Radar waveforms can be modulated with different modulation techniques to increase the performance of the radar or to add new capabilities to the radar [5, 14, 16].

A wide category of pulse compression waveforms is phase codes. Waveform characteristics are greatly determined by the coding sequence utilized, and recent radar systems use bi-phase and poly-phase coded waveforms. The phase sequencing or coding from sub-pulse to sub-pulse is designed to provoke a preferred main lobe and side lobe response in phase-coded waveforms, which have been made up of combined sub-pulses (or chips) [16]. Phase coded waveforms are generated by coding a pulse

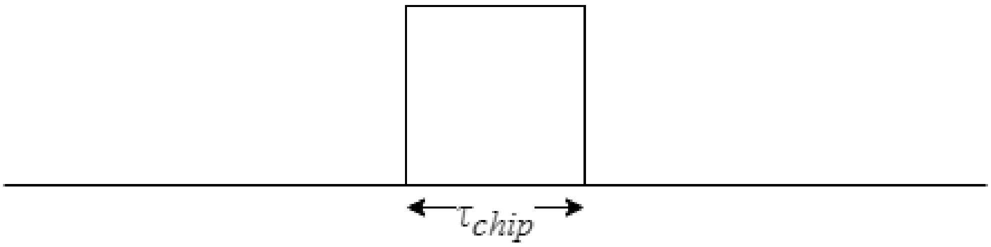

Figure 2.6 : A phase coded waveform is made up of concatenation sub-pulses or chips.

sequence consisting of sub-pulses, an example of which is shown in Fig. 2.6 and selected to generate a signal spectrum containing the main lobe and side lobe responses at the desired level. The bandwidth of the signal divided into sub-pulses is as

$$B_c = \frac{1}{\tau_{chip}}. \tag{2.8}$$

Phase-coded waveforms are generated by combining N sub-pulses and selecting the phase of each sub-pulse to obtain the desired main lobe and side lobe response at the output of a matched filter used in the radar receiver of the system. In general, side lobe levels are inversely proportional to the code sequence length. Also, long code sequences may be needed to meet SNR requirements because the energy of a phase-coded waveform is directly proportional to the waveform duration $N\tau_{\text{chip}}$. To improve range resolution, the duration of sub-pulses (τ_{chip}) can be reduced, thus reducing the energy in the waveform for a fixed-length code. Therefore, long codes may need to be used in a waveform design to meet the requirements for the waveform to have both low side lobe levels and high SNR [16, 17].

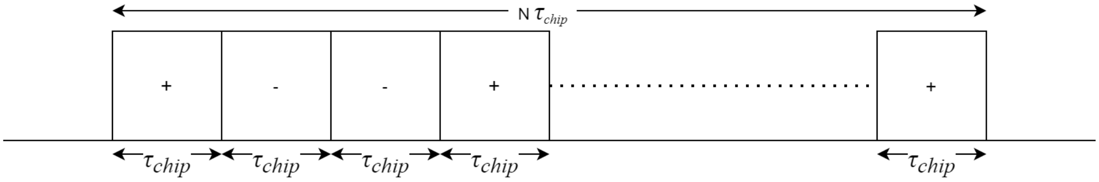

Figure 2.7 : Chips with two potential phase states compose biphase-coded waveforms.

The formulation of N subgroups that create the pulse with a total pulse width duration of τ_t is as

$$\tau_t = N\tau_{\text{chip}}\,. \tag{2.9}$$

The sub-pulses that make up this waveform in the base-band shown in Fig. 2.7 being at $\theta = 0°$ and $\theta = 180°$ phase values, and with the $e^{j\theta}$ term, amplitude values of 1 or -1.

$$a_k = e^{j\theta_k} \qquad k = 0, 1, \ldots, N-1, \tag{2.10}$$

A baseband signal created with this a_k sequence is given as

$$x_B(t) = \sum_{k=0}^{N-1} a_k g(t - k\tau_{chip}). \tag{2.11}$$

The g(t) function used represents the rect function and is expressed as

$$g(t) = \Pi\left(\frac{t - \tau_{chip}/2}{\tau_{chip}}\right). \tag{2.12}$$

If the radar transmit signal is carried to a center frequency such as f_c

$$x_T(t) = e^{j2\pi f_c t} x_B(t) = e^{j2\pi f_c t} \sum_{k=0}^{N-1} a_k g(t - k\tau_{chip}) \tag{2.13}$$

is obtained. The transmitted signal is reflected back from each object and received back with a Δt delay. If the receive signal is expressed with a delay, the resulting equation is given as

$$x_R(t) = e^{j2\pi f_c (t-\Delta t)} x_B(t - \Delta t) = e^{j2\pi f_c (t-\Delta t)} \sum_{k=0}^{N-1} a_k g(t - k\tau_{chip} - \Delta t). \tag{2.14}$$

If the received signal is downconverted a baseband, it is expressed as

$$x_{IF}(t) = e^{-j2\pi f_c \Delta t} x_B(t - \Delta t) = e^{-j2\pi f_c \Delta t} \sum_{k=0}^{N-1} a_k g(t - k\tau_{chip} - \Delta t). \tag{2.15}$$

Figure 2.8 shows an example $x_T(t)$ signal constructed using an array of elements [1, 0, 0, 1, 0, 1, 0] of length $N = 7$. In the modulation set to be in two phases, the number 0 in the array is taken as 0 degrees, while 1 π is taken as degrees.

In terms of hardware capacity, binary phase codes are easier to use than poly-phase codes. However, thanks to the developing digital wave generators, the use of polyphase

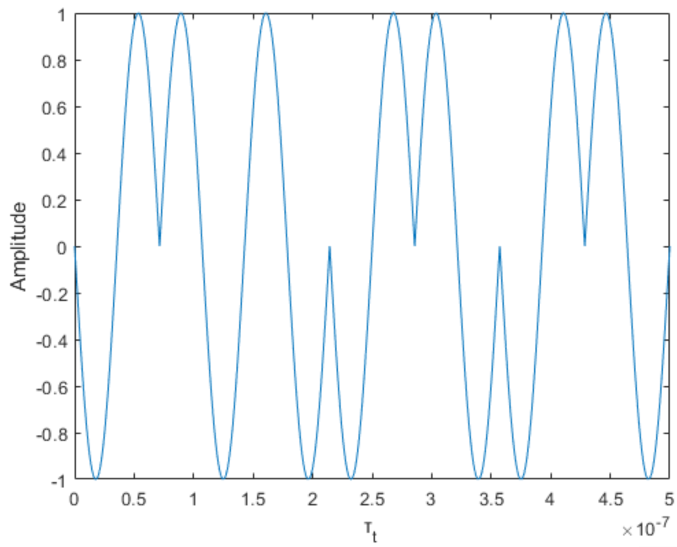

Figure 2.8 : Phase coded waveform of length $N = 7$ and one cycle carrier for each chip.

code is more likely in modern radars. The advantage of using a poly-phase encoded waveform is a lower side lobe level compared to a bi-phase code of the same length. The peak and side lobes are the most important performance parameters in a phase-modulated wave. For this reason, the code sequence can be examined by ignoring the band limitations. The auto-correlation sequence of the phase code can be written as

$$y[m] = \sum_{k=0}^{N-1} a_k a^*_{k-m} \quad m = -(N-1), \ldots, 0, \ldots (N-1). \tag{2.16}$$

Both the main lobe and side lobe levels are important performance criteria. Ignoring the effects of band limiting, the peak, and integrated side lobes can be studied using the code sequence and ignoring the chip response [16].

2.3.1 Barker codes

In its binary phase coded structure, a pulse of width τ_t is divided into smaller N parts. Afterward, the phase of each sub-pulse is randomly chosen as 0 or π radians according to the reference signal. In general, a sub-pulse with $\theta = 0$ phase is represented by the characters "1", while a sub-pulse with $\theta = 180$ phase is expressed as a shape by the characters "0" or "-1". Codes of this nature undergo pulse compression with a

Table 2.1 : All known binary Barker codes.

Code Length	Code Sequence	Peak Sidelobe Level, dB
2	$1, -1 \quad 1, 1$	-6.0
3	$1, 1, -1$	-9.5
4	$1, 1, -1, 1 \quad 1, 1, 1, -1$	-12.0
5	$1, 1, 1, -1, 1$	-14.0
7	$1, 1, 1, -1, -1, 1, -1$	-16.9
11	$1, 1, 1, -1, -1, -1, 1, -1, -1, 1, -1$	-20.8
13	$1, 1, 1, 1, 1, -1, -1, 1, 1, -1, 1, -1, 1$	-22.3

compression ratio of $\frac{\tau_t}{\tau_{\text{chip}}}$. One of the binary phase codes that produces compressed waveforms with fixed side lobe levels is the Barker code family. Barker code can have a maximum length of 13. An auto-correlation function of Barker code sequence

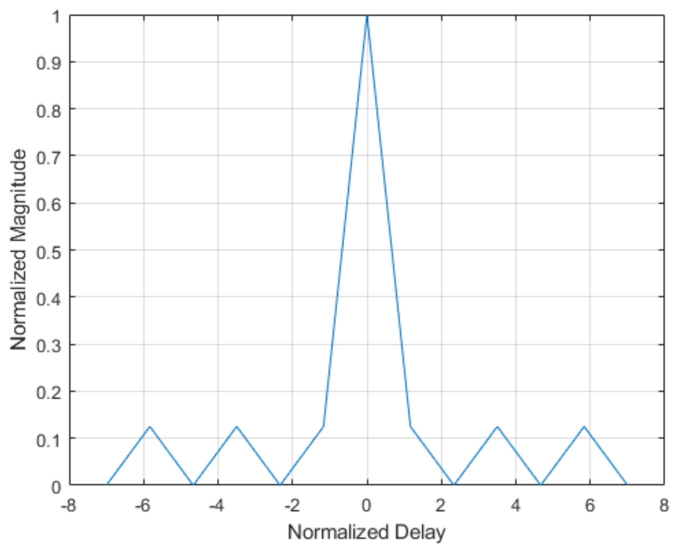

Figure 2.9 : Auto-correlation function of 7 length Barker code.

with code length $N = 7(B_7 = 1, 1, 1, -1, -1, 1, -1)$ can be seen in Fig.2.9. The rightmost column in Table 2.1 shows the ratios of the side lobe levels of the Barker code sequences [14, 16, 17].

2.3.2 Frank codes

Using another series, Frank codes, which structures using any phase with harmonic relation based on a certain fundamental phase increase can be defined as poly-phase codes. In the Frank coded, a pulse with a width of τ_t is divided into N equal groups, and then each group is divided into sub-pulses of N width τ_{chip}. The total number of sub-pulses in each pulse is expressed as N^2.

$$A = \begin{bmatrix} 0 & 0 & 0 & \cdots & 0 \\ 0 & 1 & 2 & \cdots & (N-1) \\ 0 & 2 & 4 & \cdots & 2(N-1) \\ 0 & 3 & 6 & \cdots & 3(N-1) \\ 0 & (N-1) & 2(N-1) & \cdots & (N-1)^2 \end{bmatrix}. \tag{2.17}$$

$$\emptyset_{i,j} = \left(\frac{2\pi}{N}\right)(i-1)(j-1). \tag{2.18}$$

The phases of the Frank code are obtained by multiplying the elements of the matrix A in (2.17) by the phase $2\pi/N$ when written as row 1 followed by row 2. In this matrix, j-th line i-th (2.18) is used when calculating the element phase [17–19].

The code sequence to be created for $N = 4$ is given as

$$\begin{bmatrix} 0 & 0 & 0 & 0 & 0 & \frac{\pi}{2} & \pi & \frac{3\pi}{2} & 0 & \pi & 0 & \pi & 0 & \frac{3\pi}{2} & \pi & \frac{\pi}{2} \end{bmatrix}. \tag{2.19}$$

2.3.3 P1, P2, and Px codes

P1, P2, and Px codes are all modified versions of the Frank code. The Px code was introduced by Rapajic and Kennedy in 1998 and it was shown to have a lower peak-to-side lobe ratio compared to the Frank code [17, 19]. The elements of the Px code are mathematically defined similarly to the Frank code. In this case, the phase value is given as

$$\text{Px}: \quad \phi_{i,j} = \left\{ \begin{array}{ll} \frac{2\pi}{N}[(N+1)/2-j][(N+1)/2-i], & \text{for even N values} \\ \\ \frac{2\pi}{N}[N/2-j][(N+1)/2-i], & \text{for odd N values} \end{array} \right\}. \tag{2.20}$$

The Px code sequence where $N = 4$ is shown as

$$\begin{bmatrix} \frac{9\pi}{8} & \frac{3\pi}{8} & \frac{13\pi}{8} & \frac{7\pi}{8} & \frac{3\pi}{8} & \frac{\pi}{8} & \frac{15\pi}{8} & \frac{13\pi}{8} & \frac{13\pi}{8} & \frac{15\pi}{8} & \frac{\pi}{8} \\ \frac{3\pi}{8} & \frac{7\pi}{8} & \frac{13\pi}{8} & \frac{3\pi}{8} & \frac{9\pi}{8} \end{bmatrix}. \tag{2.21}$$

The auto-correlation function of Px code sequence is shown in 2.10. P1 and P2 codes were brought to the literature by Lewis and Kretschmer. It is very similar to Px code and is derived from Frank codes. The two codes are derived based on the Frank code

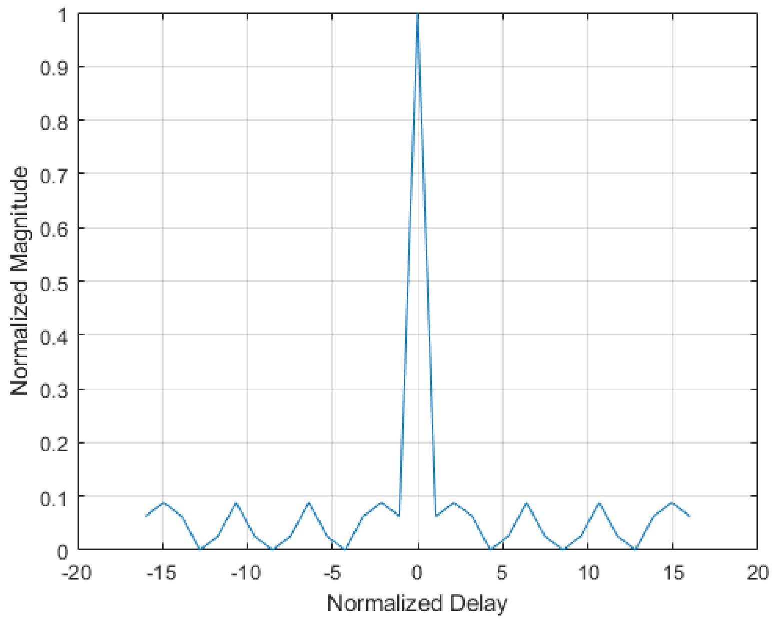

Figure 2.10 : Auto-correlation function of 16 length Px code.

and are very similar to the Px code. The length of P2 codes is also proportional to N^2, but where N is an even number in Px code sequences [17, 20]. The P1 sequence phase value is given as

$$\text{P1}: \quad \phi_{i,j} = \frac{2\pi}{N}[(N+1)/2 - i][(i-1)N + (j-1)]. \tag{2.22}$$

2.3.4 Zadoff–Chu code

The Zadoff Code(1963) sequence does not have to be N^2 in length as in frank codes and can be of any size. The r value is any prime number value with respect to N. The phase of the Zadoff Code is given as

$$\text{Zadoff}: \quad \phi_m = \frac{2\pi}{N}(m-1)\left(r\frac{N-1-m}{2} - q\right). \tag{2.23}$$

A constant phase shift can be added to all elements by changing the r and q values for any length array to be created. Chu presented an important permutation of the Zadoff code in 1972 and the phase value is given as

$$\text{Chu}: \quad \phi_m = \left\{ \begin{array}{ll} \frac{2\pi}{N} r' \frac{(m-1)^2}{2}, & \text{for even } N \text{ values} \\ \frac{2\pi}{N} r' \frac{(m-1)m}{2}, & \text{for odd } N \text{ values} \end{array} \right\}. \tag{2.24}$$

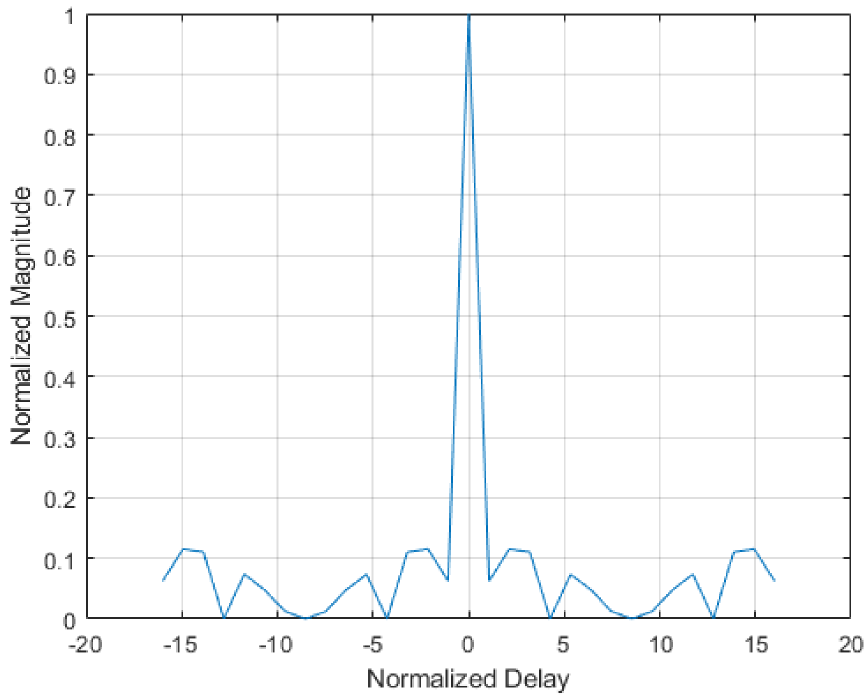

Figure 2.11 : Auto-correlation function of Zadoff-Chu code with a length of 16.

To obtain the Chu code, $r = -r$ and $q = -(M-2)r'/2$ equations are in the Zadoff code [17, 21]. For example, if a phase is calculated for $r' = 1$ or $r = -1$ and $q = 9$ to obtain an array of $N = 16$ dimensions, a result is obtained as

$$\begin{bmatrix} 0 & \frac{3\pi}{16} & \frac{\pi}{2} & \frac{15\pi}{16} & \frac{3\pi}{2} & \frac{3\pi}{16} & \pi & \frac{31\pi}{16} & \pi & \frac{3\pi}{16} & \frac{3\pi}{2} & \frac{15\pi}{16} & \frac{\pi}{2} & \frac{3\pi}{16} & 0 & \frac{31\pi}{16} \end{bmatrix}. \tag{2.25}$$

The auto-correlation function of Zadoff-Chu code sequence is shown in 2.11.

2.3.5 Pseudo-Noise codes

Bi-phase codes containing Barker codes achieve the lowest peak side-lobe for a given code sequence length. However, in many radar applications, the use of such code is not necessarily provided a good quality code with low side lobe levels is available. At this point, pseudo-random noise (PRN) codes, also known as maximum length sequences (MLS), can be used, providing predictable peak side lobe ratios approaching $10\log_{10}\frac{1}{\mathrm{N}}$ [14, 16]. When constructing a pseudo-noise (PN) sequence, the feedback shift register circuit shown in Fig. 2.12 is used and a periodic binary array is created.

This feedback shift register consists of m flip flops. These flip-flops have two state memory structures and consist of multi-loop and interconnected logic circuits. This flip-flop structure is connected to the same clock. In each incoming clock pulse, the state of the flip flops is read from the logic circuit and the Boolean function is calculated. The results are given as feedback to the first flip flop. In this way, the PN sequence is created and has a length of m, which is the length of the shift register. [22].

While k indicates the number of clock pulses, j indicates the number of flip flops, $s_j(k)$ becomes as

$$s_j(k+1) = s_{j-1}(k), \quad \left\{ \begin{array}{c} k \geq 0 \\ 1 \leq j \leq m \end{array} \right\}. \tag{2.26}$$

After the k-th clock pulse, the state of the shift register creates a cluster up to m. For the initial state, k is zero. Based on the definition of the shift register,2.26 is written.

The production of these sequences can also be expressed by the mathematical model as

$$\begin{array}{c} s_j = a_1 s_{j-1} \oplus a_2 s_{j-2} \oplus \ldots \oplus a_N s_{j-N}, \\ j = 1, \ldots, 2^m - 1 \end{array}, \tag{2.27}$$

where $s_j, s_{j-1}, \ldots, s_{j-N}$ shift register blocks correspond to feedback blocks as $\oplus$ symbol corresponds to modulo 2 addition operation.

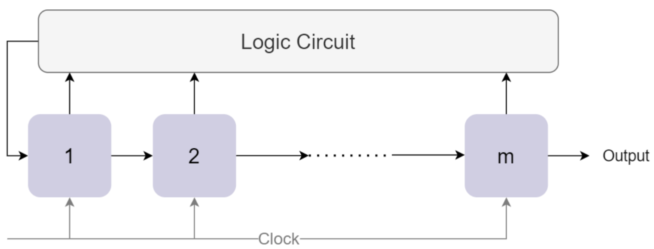

Figure 2.12 : The feedback shift register circuit.

With the shift register circuit shown in Fig. 2.12 and the length of which is expressed by the parameter m, a non-repeating code sequence of length $N = 2^{(m-1)}$ is produced. These maximum length sequences produced are periodic with the N period. These series have three main features. The properties of maximum length arrays are listed below [22, 23].

1. In maximum length arrays, the number 1 is always one more than the number 0. This property is called balance property.

2. The second property is called run property. The period formed by the numbers 1 and 0 in each cycle continues regularly as half the number of elements in the array for a one-length period, a quarter of the number of elements for a two-length period, and an eighth for a three-length period. Here, what is meant to be expressed with run are 0 and 1 which are the same periodically in a sequence. The maximum repeating period of the N-length array is $(N+1)/2$.

3. The last feature is that the auto-correlation function has periodic and binary values. The name of this property is correlation property [22, 24].

For certain m-values, N values are calculated, and for the same m-value, longer than N sequences are periodically repeated. In order to show this periodic repetition, the expression of the sequence up to T_p time with sub-sequences can be given as

$$T_p = N\tau_{chip}. \tag{2.28}$$

If this periodic signal is denoted as c(t), the auto-correlation function of the length sequence T_p is as

$$R_c(\tau) = \frac{1}{T_p}\int_{-T_p/2}^{T_p/2} c(t)c(t-\tau)dt. \tag{2.29}$$

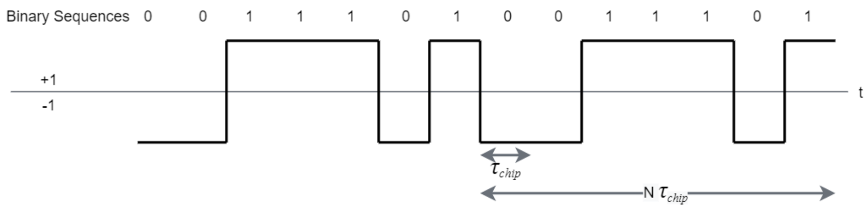

Figure 2.13 : Maximum length sequences with $N = 7$.

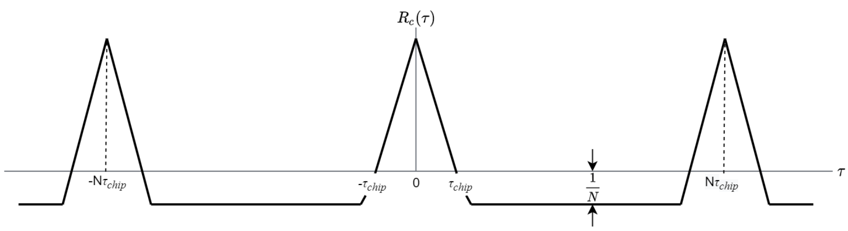

Figure 2.14 : Auto-correlation function of maximum length sequences with $N = 7$.

When $m = 3$, N takes the value 7. The sequence in this example is given in Fig. 2.13. As can be seen, each sequence element represents one subgroup. Each part of the sequence with a total length of $N \times \tau_{chip}$.The auto-correlation function of the sequence created in this way is shown in Fig 2.14 Here, it has been revealed that the third feature of PN sequences, the correlation properties, is repetitive and periodic. The auto-correlation function is as

$$R_c(\tau) = \left\{ \begin{array}{ll} 1 - \frac{N+1}{N\tau_{chip}}|\tau|, & |\tau| \leq \tau_{chip} \\ -\frac{1}{N}, & \text{for the remainder of the period} \end{array} \right\}, \tag{2.30}$$

when the $c(t)$ value is adjusted [22].

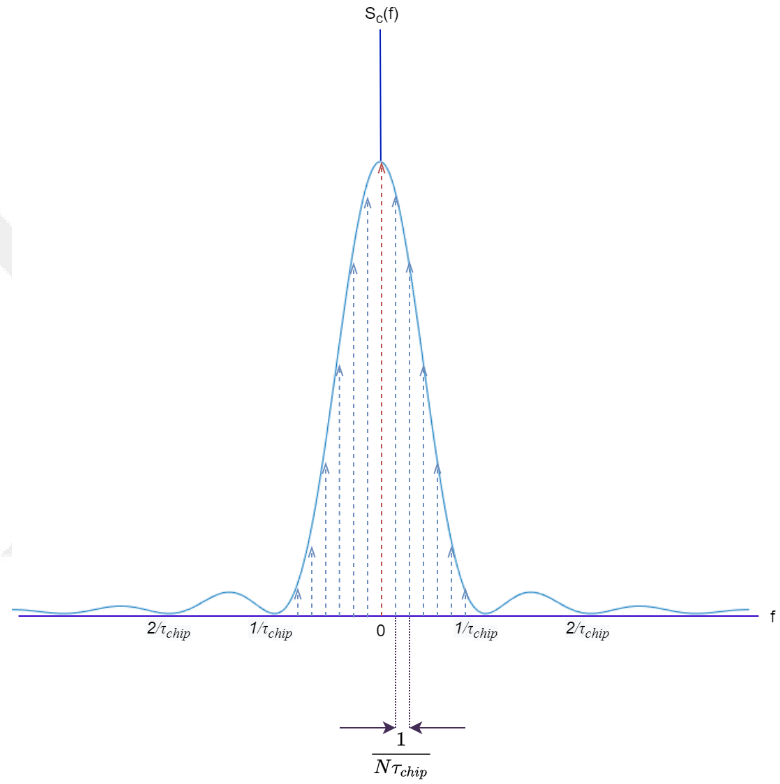

Figure 2.15 : The power spectral density of the maximum length array with $N = 7$.

Periodicity in the time domain is converted to sampling in the frequency domain. This interaction between the time and frequency domains is revealed by the power spectral density of the maximum-length array waveform $c(t)$. When the Fourier transform of the auto-correlation function $R_c(\tau)$ given by the expression in (2.30) is taken, the power spectral density of $c(t)$ is obtained. The mathematical expression related to this is given as

$$S_c(f) = \frac{1}{N^2}\delta(f) + \frac{1+N}{N^2} \sum_{\substack{n=-\infty \\ n\neq 0}}^{\infty} \text{sinc}^2\left(\frac{n}{N}\right)\delta\left(f - \frac{n}{N\tau_{chip}}\right), \tag{2.31}$$

Table 2.2 : The polynomial ($h(x)$) of pseudo noise sequences.

Number of Stages (m)	Feedback Coefficients	h(x) Polynomial
2	111	x^2+x+1
3	1011	x^3+x+1
4	10011	x^4+x+1
5	100101	x^5+x^2+1
6	1000011	x^6+x+1
7	10001001	x^7+x^3+1
8	100011101	$x^8+x^4+x^3+x^2+1$
9	1000010001	x^9+x^4+1
10	10000001001	$x^{10}+x^3+1$
11	100000000101	$x^{11}+x^2+1$
12	1000001010011	$x^{12}+x^6+x^4+x+1$
13	10000000011011	$x^{13}+x^4+x^3+x+1$

and the graph is given in Fig.2.15 [22, 24].

$$h(x) = d_N x^N + d_{N-1} x^{N-1} + \cdots + d_1 x + 1 \tag{2.32}$$

Shift register circuits in 2.12 provide feedback with blocks in the circuit, each corresponding to values 0 or 1. The feedback coefficients are obtained from a non-simplified polynomial specified in the equation. The d_k coefficients in the polynomial in (2.32) are 0 or 1, and these coefficients are equal to the coefficients of the shift register circuit in the mathematical model in equation (2.27) [16, 22]. For example, the polynomial $h(x)$ describing the feedback connections of the shift register circuit of length $N = 4$ is a 4-th order polynomial, which can be defined as $h(x) = x^4+x+1$. Feedback shift register circuits have at least 2 feedback connections. In fact, it can take more than one polynomial after the 5-th order. However, a single polynomial example is given in each order to make the table simpler. This given example is the most optimized polynomial. To illustrate this, a Table 2.3 with only polynomial coefficients and which can take more than one polynomial value is given.

To give an example, two different configurations of the shift register for $m = 5$ are shown in Fig. 2.16. For the first feedback structure in 2.16 (a), the [2 5] configuration from Table 2.3 is selected. For the second configuration in 2.16 (b), [2 3 4 5] configuration is selected from Table 2.3.

Table 2.3 : Coefficients for polynomial $h(x)$.

Number of Stages (m)	Length of Sequence (N)	$h(x)$ Polynomial Coefficients
2	3	[1,2]
3	7	[1,3]
4	15	[1,4]
5	31	[2,5], [2,3,4,5], [1,2,4,5]
6	63	[1,6], [1,2,5,6], [2,3,5,6]

Obviously, the [2 5] configuration is more advantageous as it has less feedback structure. Assuming that the binary values of the blocks in the circuit are 10000 at the beginning, the pseudo-random code sequence circuit in Fig. 2.16 is generated as a result of a period of 31 iterations. Because after the 31st iteration, the binary values of the blocks in the circuit again become 10000 [22]. The first 31 rows in column 5 in Table 2.4 contain the binary values of the pseudo-random code sequence produced by the register circuit. From this, it can be said that the pseudo-random code sequence produced is in the form 0000101011101100011111001101001 [22].

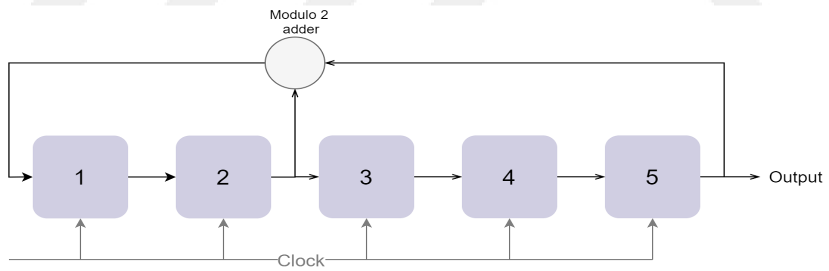

(a)

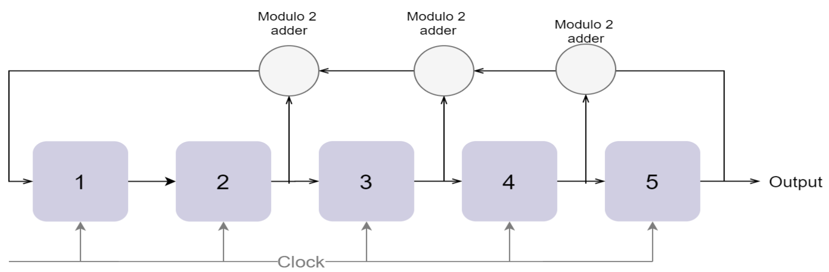

(b)

Figure 2.16 : Two different configurations of the shift register for $m = 5$.
(a) $h(x)$ polynomial coefficients [2 5]. (b) $h(x)$ polynomial coefficients [2 3 4 5].

Table 2.4 : The way a 5-block linear feedback shift register circuit generates a pseudo-random code sequence with a code length of 31.

Number	Binary values of blocks					Output
of Iterations	1	2	3	4	5	$2 \oplus 5$
1	1	0	0	0	0	0
2	0	1	0	0	0	1
3	1	0	1	0	0	0
4	0	1	0	1	0	1
5	1	0	1	0	1	1
6	1	1	0	1	0	1
7	1	1	1	0	1	0
8	0	1	1	1	0	1
9	1	0	1	1	1	1
10	1	1	0	1	1	0
11	0	1	1	0	1	0
12	0	0	1	1	0	0
13	0	0	0	1	1	1
14	1	0	0	0	1	1
15	1	1	0	0	0	1
16	1	1	1	0	0	1
17	1	1	1	1	0	1
18	1	1	1	1	1	0
19	0	1	1	1	1	1
20	0	0	1	1	1	1
21	1	0	0	1	1	1
22	1	1	0	0	1	0
23	0	1	1	0	0	1
24	1	0	1	1	0	0
25	0	1	0	1	1	0
26	0	0	1	0	1	1
27	1	0	0	1	0	0
28	0	1	0	0	1	0
29	0	0	1	0	0	0
30	0	0	0	1	0	0
31	0	0	0	0	1	1

3. NOISE RADAR SYSTEM MODEL

The working logic of the near field digital coded radar system, which is designed and simulated, is basically, after a digital coded radar waveform is produced by the transmitter of the system and propagated by its antenna towards the target in the near area, the waveform scattered from the target is detected by the antenna and this echo signal is demodulated by the receiver. It is based on the detection of the target's range information. The range information of the target is based on the receiver structure of the radar system. It is obtained as a result of processing the signal at the output. In the signal processing structure of the system, the signal processing algorithm works to determine the range of the target. These signal processing algorithms can be programmed in field programmable gate arrays (FPGA) circuits used in radar systems. In this thesis, in this part of the thesis, the receiver and signal processing structures of the digital coded radar system are explained and the signal processing algorithm for extracting the range of the target is created. This algorithm was written and simulated in the MATLAB program.

3.1 Radar Receiver

The radar receiver subsystems of the designed radar system are shown in Fig. 3.1. The signal entering RF receive block with the signal coming from the RF receive antenna. Then the RF receive block is digitized by passing through the ADC and the signal is proccesed in correlation block. Finally, it enters the delay calculation block to obtain range information [25].

Modern radar systems usually have a low noise amplifier (LNA) at the receiver input. In this way, the noise figure is tried to be reduced. Then, with the help of the band-pass filter, the signals outside the operating frequency band are eliminated. The signal passing through the filter is downconverted to intermediate frequency (IF) in the mixer

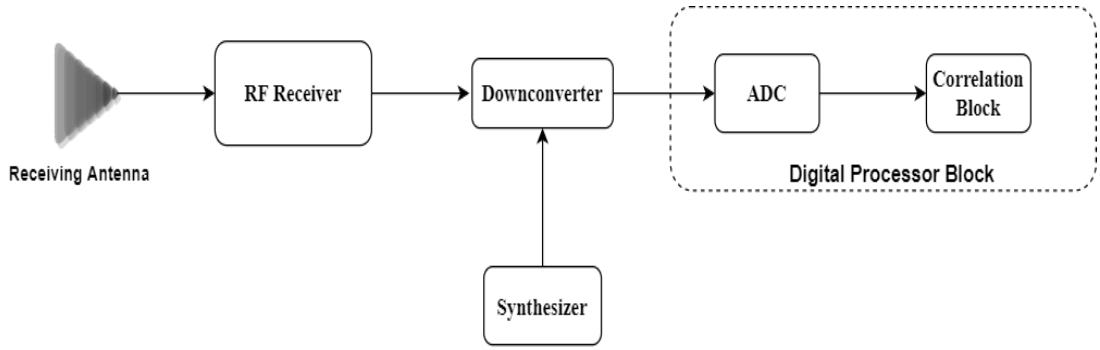

Figure 3.1 : The block diagram of radar receiver.

with the help of the local oscillator (LO) signal. The power of the signal at the mixer output is amplified with the help of an amplifier. Undesirable parts of the signal passing through the narrowband filter used are eliminated. Following that, the receiver subsystem's output is determined by the detection of the intermediate frequency signal. The radar video signal is the name given to the final receiver outputs. A video signal is a signal received after all carrier or intermediate frequencies have been eliminated in radar [16, 25].

Because there are sensitive components in the input structure of an RF receiver, it must be protected against high-power input. There must be an isolating structure to protect from this emitted energy during the broadcasting period. In addition, since high incoming signals will saturate the RF structure, it may be difficult to detect targets in the near field. Therefore, a front-end block is used after the antenna of the RF input. If a single antenna is to be used in the system, this structure is placed in the T-R module. If the receiving and transmitting antennas are to be different, this structure is placed directly behind the receive antenna, physically close to it. The reason why it is close is that the receiver block does not lose its sensitivity due to the losses caused by the RF line.

In the input block of RF receiver structures, preselector blocks are generally used to prevent interference signals. Because interference signals are an important issue for RF receiver systems and must be prevented. At the same time, interference effects can come from different frequency sources. These can also be jammer signals. For barrage noise-type jammers, the jamming signal is spread out in frequency so that only a portion of the jamming signal is within the bandwidth of the desired radar signal. a filter block is inside the preselector structure. The signal passing through this filter block is minimized from being affected by other frequencies. After the echo signal is amplified in the RF section, it is mixed with the local oscillator frequency and shifted to an intermediate frequency. Mixers that do this act as multipliers, producing an output proportional to the product of the two input signals. When the RF signal with frequency f_{RF} and local oscillator signal with the frequency f_{LO} is input into the mixer, the reduction to $f_{IF} = f_{RF} - f_{LO}$ frequency is realized at the mixer output. The conversion process of the echo signal from RF to IF through the mixer.

Today, most radar systems use digital signal processing to perform the functions of detecting, tracking, and displaying targets in range, although the radar signals are analog. At this point, there are ADC structures in radar systems in order to convert analog signals to digital signals. Many modern radar receivers include the ADC part that provides digital signals by directly converting IF components to digital format as a result of the sampling process to detectors with processors running signal processing algorithms. Advances in resolution, speed, and cost in ADC and digital signal processing technologies make a significant contribution to receiver designs in digital coded radar systems and popularize the use of digital receivers instead of analog receivers. The selection of the ADC sampling rate, which is an important parameter in preventing the disturbing effect of unwanted signal and noise components, is determined according to the IF bandwidth. A band-limited IF signal that is not in the baseband can be sampled as long as the sample rate of the signal is at least twice the bandwidth. According to the Nyquist sampling theorem, each signal or channel is sampled at a rate equal to or more than twice the highest frequency component. For a baseband-centered band-limited signal, the highest frequency is equal to half the bandwidth. Therefore, the ADC must sample at a rate equal to or greater than the waveform bandwidth. Bandpass filters in the radar system receiver structure are designed with a bandwidth equal to the bandwidth of the radar waveform and remove the signals outside this frequency band [16]. Sampling, which is a basic operation for digital signal processing and digital communication and is explained by the Nyquist theorem, is usually defined in the time domain. Through the sampling process, an analog signal is converted into a corresponding sample sequence that is uniformly spaced over time. For this process to take place properly, the sampling rate must be chosen following the bandwidth of the signal [22]. Considering the Nyquist theorem, the sampling rate f_s and the sampling interval T_s of the ADC that is performed the sampling operation in f_{IF} should be determined according to the criterion in the expression specified as

$$f_s = \frac{1}{T_s} > 2B. \tag{3.1}$$

3.2 Radar Transmitter

The radar transmitter block consists of a PN generator, up-converter, synthesizer, and power amplifier blocks. Radar transmitters are the most important block of the instantaneously high-power radar system. For the radar system to be effective, an RF signal with the desired bandwidth and frequency must be able to output in this block. Fig. 3.2 shows the radar transmitter block in the system used. In the digital processor

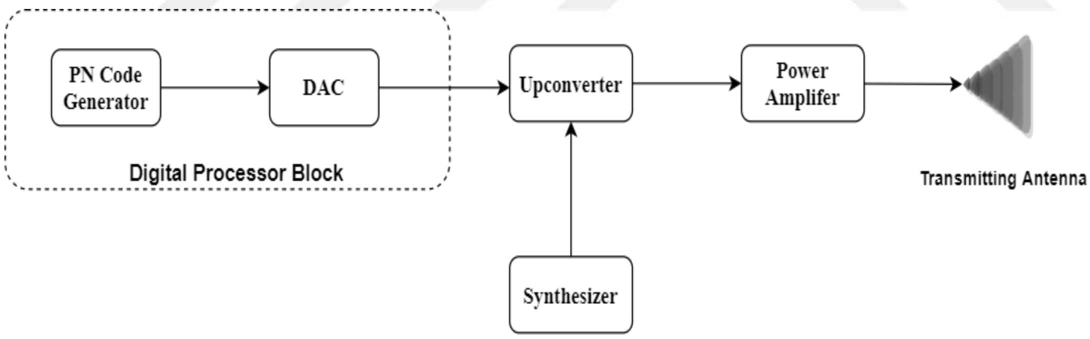

Figure 3.2 : The block diagram of radar transmitter.

block, PN code is generated as in Fig. 2.12 an IF output is obtained by analogizing it at the DAC output.

This IF output is amplified to RF with the help of a synthesizer and up-converter. While doing this process, mixers in the synthesizer block are used. The synthesizer block is the same as the receiver and transmitter blocks. Because the frequency down-converting and up-converting blocks work synchronously. The signal amplified to the RF frequency is passed through the power amplifier and the signal with the increased power is broadcast with the help of the antenna [16].

3.3 Radar Platform

While the radar platform was being designed, it was planned to be placed on a rotary wing unmanned aerial vehicle (Drone). Radar subsystems will be added to the payload part of this vehicle. With this drone system, which is at a certain level above the air, it will be possible to extract the range profile of the radar target from the desired angle and distance.

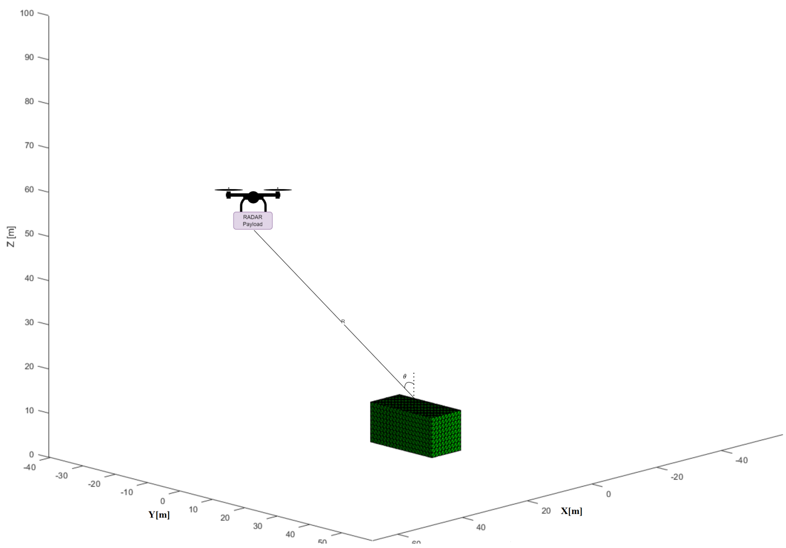

Figure 3.3 : Radar platform on drone and target model.

As seen in Fig. 3.3, the radar platform integrated on the drone is at a distance R from the object and makes θ angle with the surface normal. It is possible to infer the range profile from different positions of the radar. Radar image can also be extracted by collecting information from more than one position of the radar.

3.4 Targets' Reflection Characteristics

The first descriptions of a goal had been in terms of a single cross-sectional area valued at a certain amount. This amount is generally some kind of average cross-section over the most likely aspect angles, as determined by the system designer. As a result of this method, system designers are able to correlate a single cross-sectional area of constant value with a goal, resulting in the steady-state target model. Following this approach, models are built to provide a signal-to-noise ratio that has been rather arbitrarily determined at a specified maximum operational range. The underlying principle is that even if this aim is accomplished, the needed detection capability and parameter estimate accuracy can be obtained. The human observer's major position in early detection systems made this technique acceptable [26].

The size and type of the target external surfaces to the radar beam have a big impact on the echo characteristics. Because the incident wavelength is too long to distinguish target details, the variation is negligible for electrically small targets (targets smaller than a wavelength in size). The flat, singly curved, and doubly curved surfaces of electrically large objects, on the other hand, all produce various echo characteristics [5]. There are multiple RCS calculation methods. The method to be used in this study is physics optics methods. These include theories of optics, geometric and physical theories of refraction and the method of equivalent currents. RCS calculation is obtained by finding the electric field scattered from a target in the forehead. Simply expressed, RCS is the ratio of "per unit solid angle of power reflected to the receiver" to "density of incident power /4π". The RCS (σ) formulation is expressed as

$$\sigma = \lim_{R\to\infty} 4\pi R^2 \frac{\left|\vec{E}_s\right|^2}{\left|\vec{E}_i\right|^2} \tag{3.2}$$

where the transmitted electric field is E_i and the back-scattered electric field is E_s [27]. In RCS estimation methods, scattering from the body is defined for three different regions. While determining these three regions, the comparison of the wavelength for the object length is considered.

While most approximation techniques have been created for the optical area, also known as the high-frequency region, the accurate approaches are limited to relatively simple or tiny objects in the Rayleigh and resonant zones. Of course, there are exceptions to these basic restrictions. If one employs sufficiently precise math, one may utilize the exact solutions for many items for huge bodies far into the optics area, and many optics approximations can be extended to entities with moderate electrical sizes into the resonance zone. The Rayleigh area's low-frequency approximations can be extended upward into the resonance region. RCS estimation methods in the optic region have their advantages and disadvantages. Among these methods, the most widely used methods are physical optics and geometric optics methods. These methods are effective for electrically large objects. [5, 27].

The physics-optic method, is a suitable method for flat and slightly curved bodies. The far-field approximation posits that the distance between the scattering object and the point of view is considerable in comparison to any dimension of the obstruction.

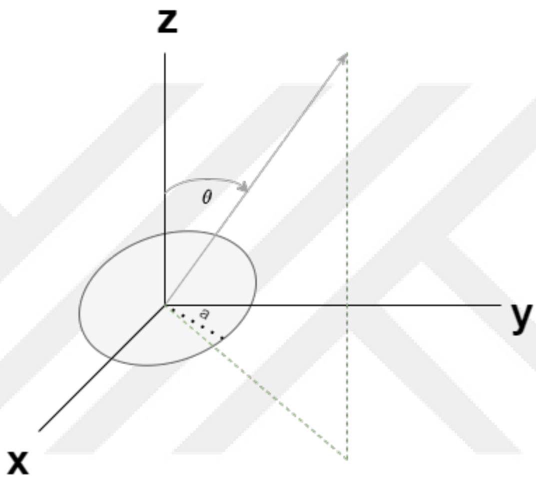

Figure 3.4 : Circular metal disc.

If the areas of the circular and rectangular metal disk are $0.125m^2$ and the frequency is 10 GHz,then the RCS value of the circular and rectangular metal disc are calculated, Fig. 3.5 is obtained in logarithmic scale. The physical optics approach for a metallic plate is relatively simple because the phase value in the integral is the only variable and this phase value changes linearly across the surface. In this case, if the surface area $A = \ell w$ is accepted and the θ value is accepted as the angle between the surface normal and the radar platform, the RCS value of the rectangular metal plate is as

$$\sigma = 4\pi \left| \frac{A\cos\theta}{\lambda} \cdot \frac{\sin(k\ell\sin\theta\cos\phi)}{k\ell\sin\theta\cos\phi} \cdot \frac{\sin(kw\sin\theta\sin\phi)}{kw\sin\theta\sin\phi} \right|^2 . \tag{3.3}$$

Since the RCS value to be used in this study is taken into account for the circular metal disc like in Fig 3.4, the RCS of this disc is calculated. If the RCS value is desired to be

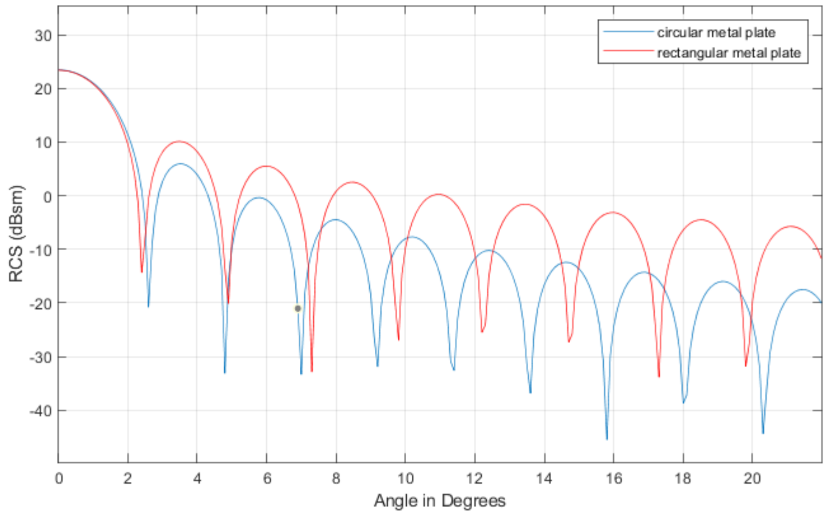

Figure 3.5 : RCS for a circular metal disc and rectangular metal disc.

obtained by comparison, the result is obtained as

$$\sigma = 4\pi k^2 a^2 \left(\cos\theta \frac{J_1(2ka\sin\theta)}{2k\sin\theta} \right)^2, \tag{3.4}$$

where $J_1(x)$ gives the 1st order Bessel function, where a is the radius, k is the wave number. [5, 27].

4. SIMULATION RESULTS & ANALYSES

The simulation of the signal processing algorithm of the designed radar system, which is based on the correlation of the signal scattered from a target in the near range area and the digitally coded signal produced in the radar transmitter, has been made in the MATLAB program. While generating the transmitting signal, the PN code series is used in the phase modulation of the digitally coded radar.

4.1 Range Profile of Scattering Points

In this context, within the framework of the working scenario, it is assumed that there are 4-point target objects at the distances determined in the x coordinate axis among the targets within the range of the radar, whose position in the Cartesian coordinate system is accepted as $(50,0,0)$. The locations of the determined objects in the coordinate axes are given in Table 4.1. The scenario with radar and objects are shown in Fig 4.1.The position of the radar $(50,0,0)$ and the positions of the targets appear as $(100,0,0)$, $(150,0,0)$, $(300,0,0)$ and $(400,0,0)$ respectively.

The designed radar system consists of a transmitter and a receiver. The signal produced in the transmitter part is a digitally coded waveform containing the PN code sequence. In MATLAB, the 10th order $h(x)$ polynomial, which defines the feedback connections of the shift register circuit with length $m = 10$, is formed as $x^{10} + x^3 + 1$ considering the coefficients in Table 2.2, $N = 1024 - 1 = 1023$ with length PN code sequence is generated. The waveform is expressed as

$$x_T(t) = e^{j2\pi f_c t} \sum_{k=0}^{N-1} a_k g(t - k\tau_{chip}), \tag{4.1}$$

where it contains this generated code sequence with a frequency of $f_c = 10GHz$ and where $g(t) = \Pi\left(\frac{t-\tau_{chip}/2}{\tau_{chip}}\right)$.

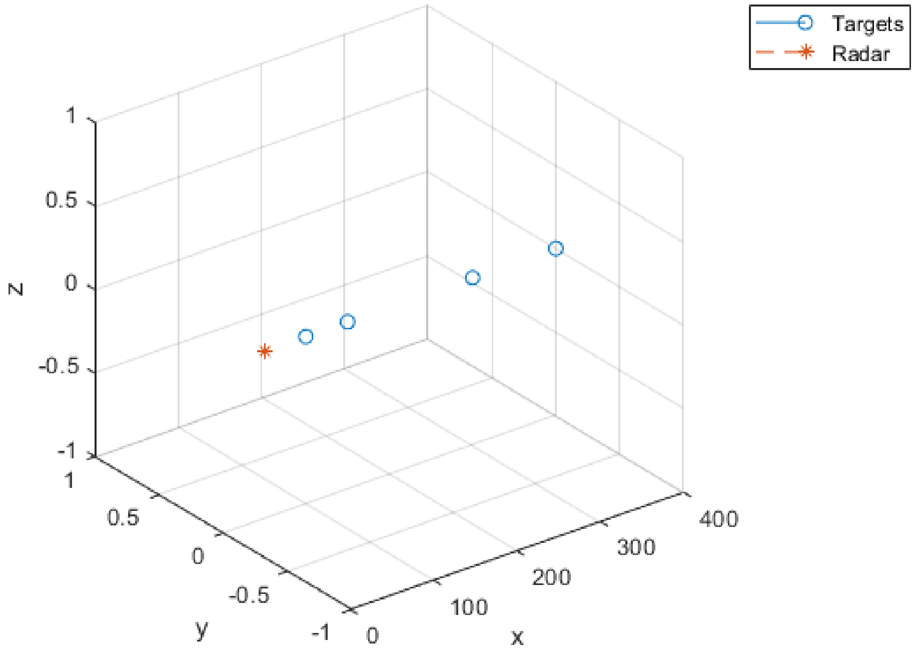

Figure 4.1 : Radar and target locations.

Table 4.1 : Positions and velocities of scattering points..

x	y	z	RCS	Vx	Vy	Vz
100	0	0	1	0	0	0
150	0	0	1	0	0	0
300	0	0	1	0	0	0
400	0	0	1	0	0	0

a_k gives the coefficients of the PN series, which takes the value 1 or -1 with phase value $0°$ or $180°$. The width of each sub-pulse, which has $N = 1023$ sub-pulses, is calculated with the formula specified as

$$\tau_{\text{chip}} = \frac{\tau_t}{N} = \frac{50\,us}{1023} \cong 48.876\,ns, \tag{4.2}$$

with the sampling interval T_s specified as

$$T_s = \frac{1}{f_s} = \frac{1}{250\text{MHz}} = 4\text{ns}. \tag{4.3}$$

The zoomed version is given in Fig. 4.2 to observe the phase change in the $x_T(t)$ transmit signal. The Fourier transform of the $x_T(t)$ signal is applied to determine the frequency components of the $x_T(t)$signal in the generated time domain. With

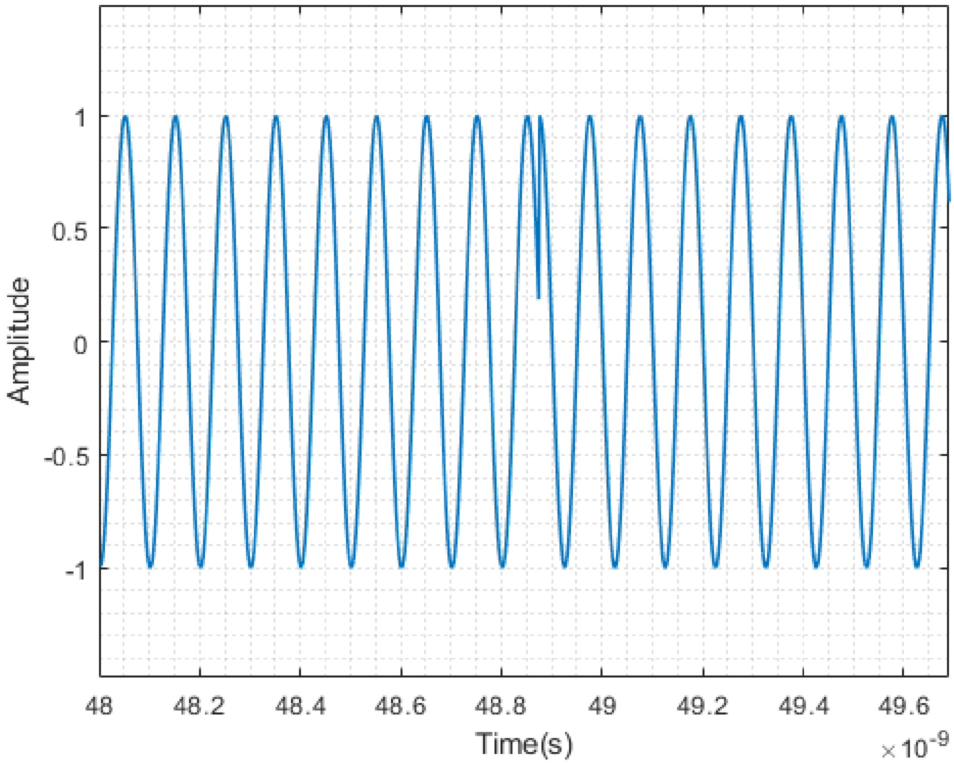

Figure 4.2 : Zoomed digital coded waveform in the radar transmitter signal ($x_T(t)$).

the Fourier transform, a signal is transferred from the time domain to the frequency domain.

The signal in Fig. 4.3 is obtained by applying the FFT process to the $x_T(t)$ signal in MATLAB.

While obtaining the filtered FFT form of the $x_T(t)$ signal in Fig.4.3 as normalized and logarithmic, the bandwidth of the designed and simulated radar system is determined according to the rule specified as

$$f_s > 2BW, \tag{4.4}$$

and filtered so that it remains around the base-band frequency.

In order to shift the signal to the baseband, the f_{LO} frequency is selected as the same as the center frequency, with the f_{IF} frequency being zero. The sampling frequency f_s is selected as $250\,$MHz, taking into account (4.4).

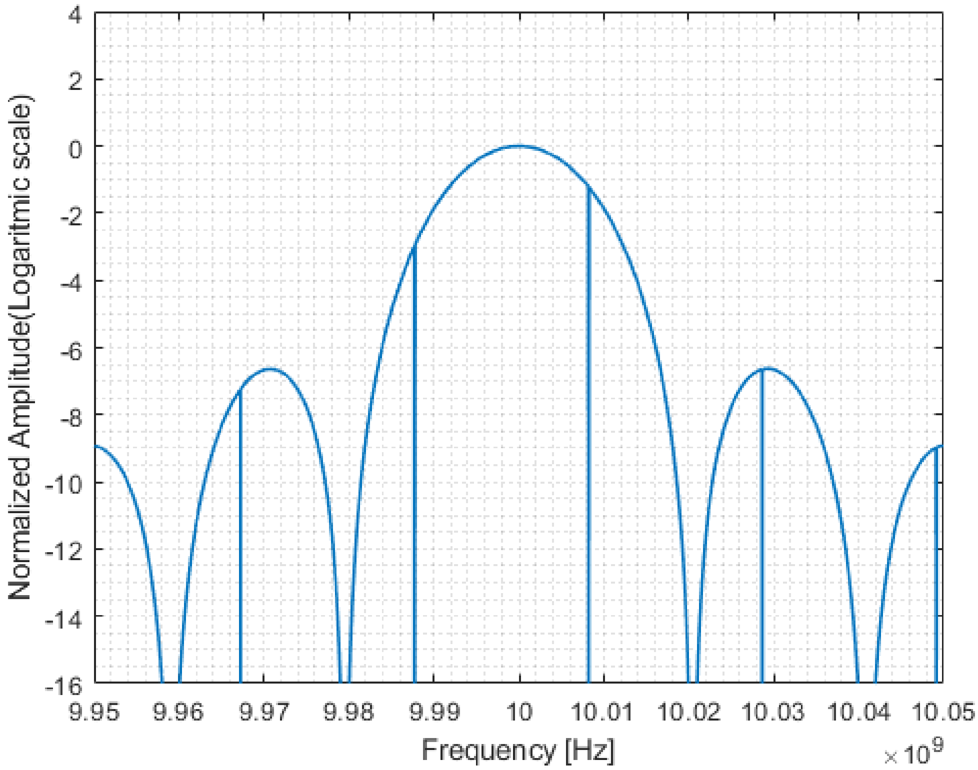

Figure 4.3 : FFT of the radar transmit signal.

The bandwidth of the generated signal is directly related to the length of the PN array. The code length determines the duration of each τ_{chip}.

The bandwidth of the transmit signal is calculated as

$$B = \frac{2 \times N}{\tau_T}. \tag{4.5}$$

Since $N = 1023$ and $\tau_t = 50\,us$, the bandwidth is calculated as approximately $40\,$MHz. The $40\,$MHz bandwidth is shown in Fig.4.3, which is the graph of the signal after the FFT is received.

The digital coded $x_T(t)$ signal created in the radar system's transmitter structure is scattered from the target after it is sent to the targets within the radar's range, and is received by the receiver structure of the system with a certain delay time. The range profile information of the targets is subtracted from the delay times. In this context, the signal model is created based on the superposition principle as a result of scattering from multiple targets in the receiver part of the designed and simulated numerically coded radar system is given as

$$x_R(t) = \sum_{m=1}^{M} \sigma(m) e^{j2\pi f_c(t-\Delta t_m)} \sum_{k=0}^{N-1} a_k g(t - k\tau_{chip} - \Delta t_m). \quad (4.6)$$

where the parameter M represents the number of targets in the radar's range and σ is the RCS value of the target, and the Δt parameter expresses the delay time of the echo coming from the target to the receiver of the radar. For point scatterers, the RCS value is fixed and 1 is selected. The signal from the radar is multiplied by an $LO = f_c$

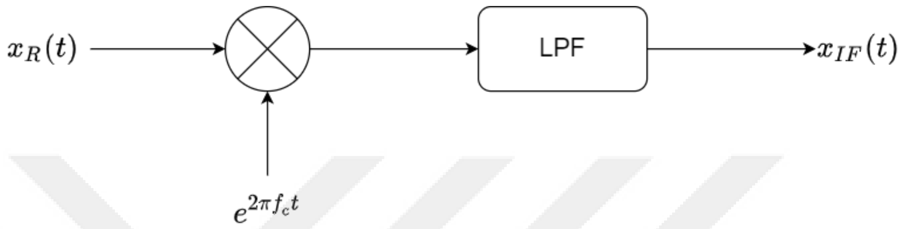

Figure 4.4 : Block diagram of downconverting the receiving signal to base band .

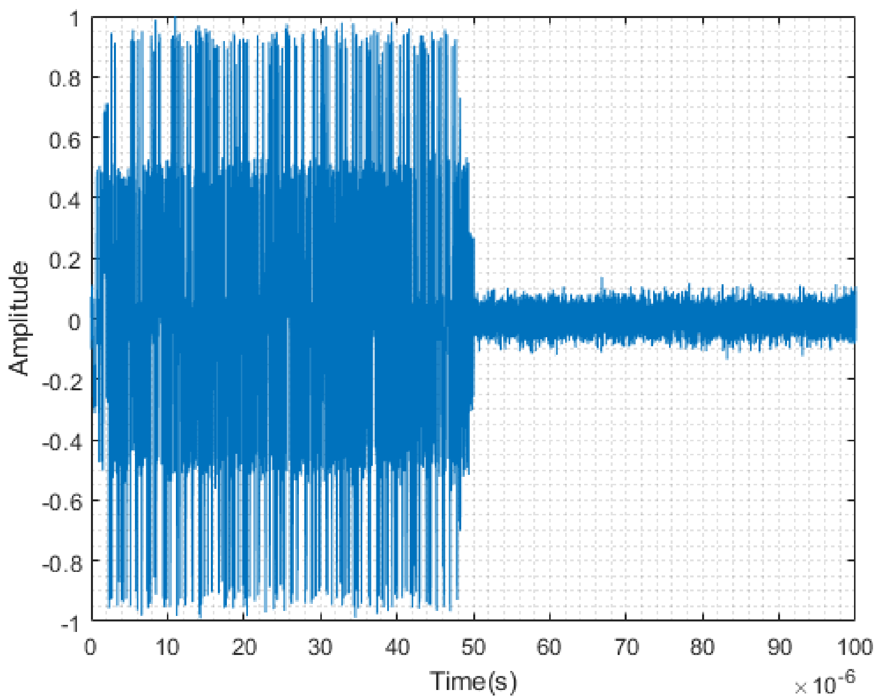

Figure 4.5 : The radar receiver signal with noise ($x_R(t)$).

frequency and lowered into the base band as in Fig. 4.4. The LO frequency is selected the same as the RF frequency.Then, the base band signal is obtained by passing it through a low pass filter and expression of the $x_{IF}(t)$ signal is given as

$$x_{IF}(t) = \sum_{m=1}^{M} \sigma(m) e^{-j2\pi f_c \Delta t_m} \sum_{k=0}^{N-1} a_k g(t - k\tau_{chip} - \Delta t_m). \tag{4.7}$$

White Gaussian noise with zero mean variance is generated in MATLAB to model the thermal noise produced in the radar receiver. The noisy $x_R(t)$ signal was obtained in MATLAB as a result of adding the 10dB level form of the SNR value of the radar system, which is shown in Fig. 4.5. In the radar transmit pulse signal, constant t_{PRI} is selected and this value is chosen as $100us$. In the signal processing part of the

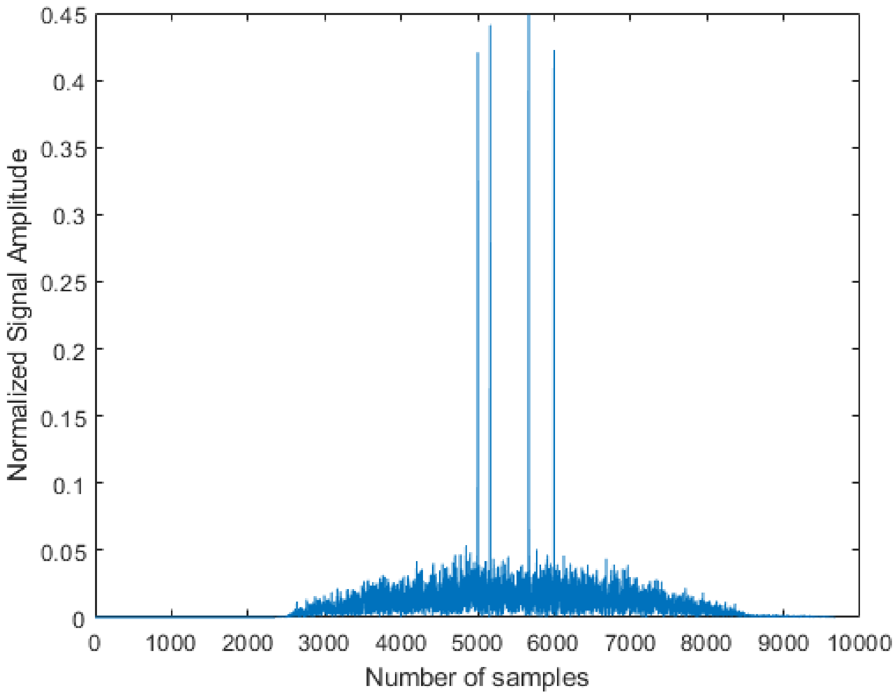

Figure 4.6 : The cross-correlation of multi-target noisy $x_R(t)$ and $x_T(t)$.

simulated digital coded radar system, a correlation-based signal processing algorithm is used to detect the range information of the targets. With the implementation of this algorithm in MATLAB, the delayed time information of the transmitted signal in the base-band, which is created in the transmitter structure of the radar system, of the targets in the signal in the base-band, which is received with noise, is determined. As a result of cross-correlation of the band-limited multi-target Fig. 4.6 is obtained. The signal formed as a result of the cross-correlation in the waveform in Fig. 4.6 contains samples equal to one less than twice the number of samples of the $x_T(t)$ and $x_R(t)$ that entered the cross-correlation process. As a result of applying the cross-correlation algorithm in MATLAB, the number of samples of the signal obtained in Fig. 4.6 is 9667. it is clearly seen that, looking at the signal in Fig. 4.6, there are peak values at four points. These peak values give information about the targets within the range of the radar.

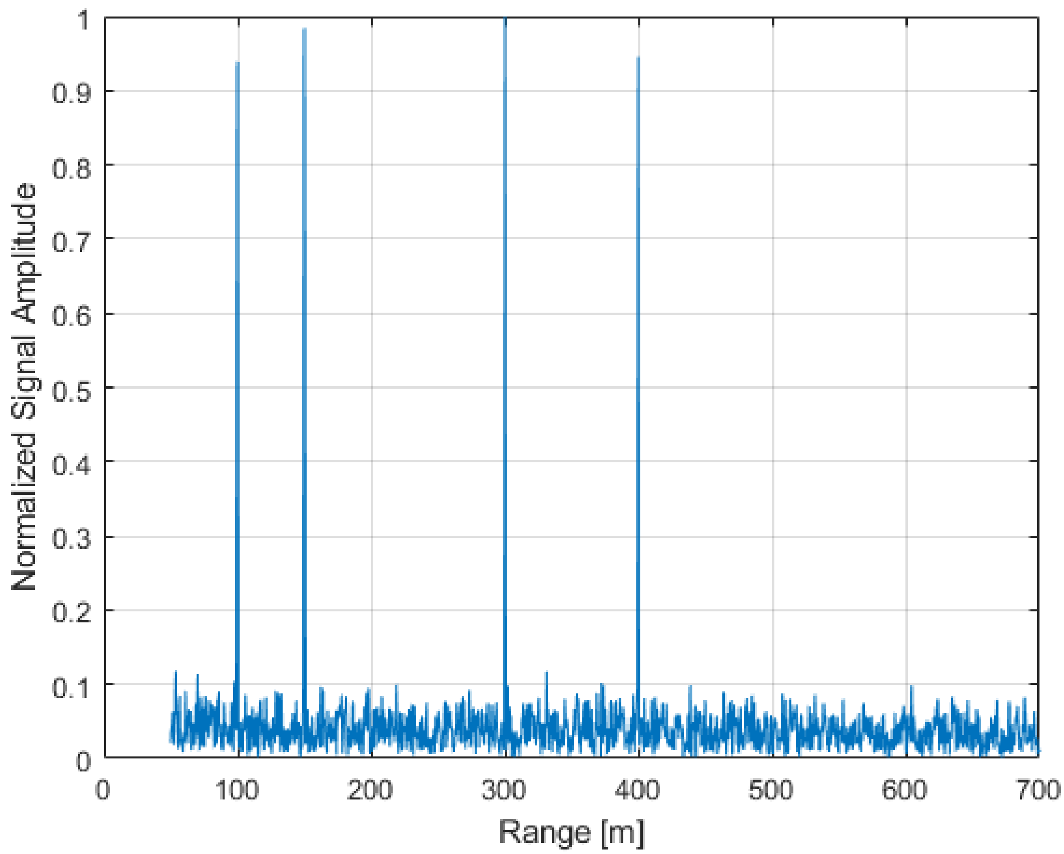

Figure 4.7 : Phase coded radar range profile.

When the processes are continued in this way and the range profile image is extracted, Fig. 4.7 is obtained. As can be seen from the Fig. 4.7, 4 different targets are located at 100, 150, 300 and 400 meters. The digital phase coded radar system, designed and simulated with the system parameters specified in Table 4.2, detects the targets within its range as a result of the decision of the detector structure in the signal processing part.

Table 4.2 : The digital phase coded radar system parameters.

System Parameters	Values
Radar Position Coordinates	(50, 0, 0)
Number of Targets	4
First Target Position Coordinate	(100, 0, 0)
Second Target Position Coordinate	(150, 0, 0)
Third Target Position Coordinate	(300, 0, 0)
Fourth Target Position Coordinate	(400, 0, 0)
Carrier Frequency	10 GHz
Center RF Frequency	10 GHz
Sampling Frequency	250 MHz
Pulse width	50 us
PN Code Length	1023
Bandwidth	40 MHz
Range Resolution	0.73 m
Signal to Noise Ratio	10 dB

4.2 Range Profiles with Different PN Code Lengths

The bandwidth of the generated signals changes when the size of the PN array used is changed. At the same time, the size of each sub-pulse of the generated signal also changes. More precise range profile results are obtained when using transmit signals generated with longer series. In order to make this comparison, as seen in Table 4.3, the lengths of the PN sequence used in phase modulation are given as $N = 16, 32, 64, 128, 256$ and 512, respectively.

As can be seen in Fig. 4.8, bandwidths of six different lengths of PN series are given. Considering the main lobe, it is seen that the smallest value is at $N = 16$ and the largest bandwidth value is at $N = 512$. Bandwidths are observed to be approximately $0.6, 1.24, 2.5, 5, 10.2$ and 20.44MHz for $N = 16, 32, 64, 128, 256$ and 512 respectively. In Fig. 4.9, there are range profiles created by the correlation method. For example, as can be seen in Fig. 4.9(a), if a PN series with $N = 16$ is used, the location of four points in the range profile cannot be distinguished exactly. Again, as the N number increases, it is seen that the spot scatterers are more uniform in the range profiles. If these six range profiles are compared, the most exact range profile is Fig. 4.9(f).

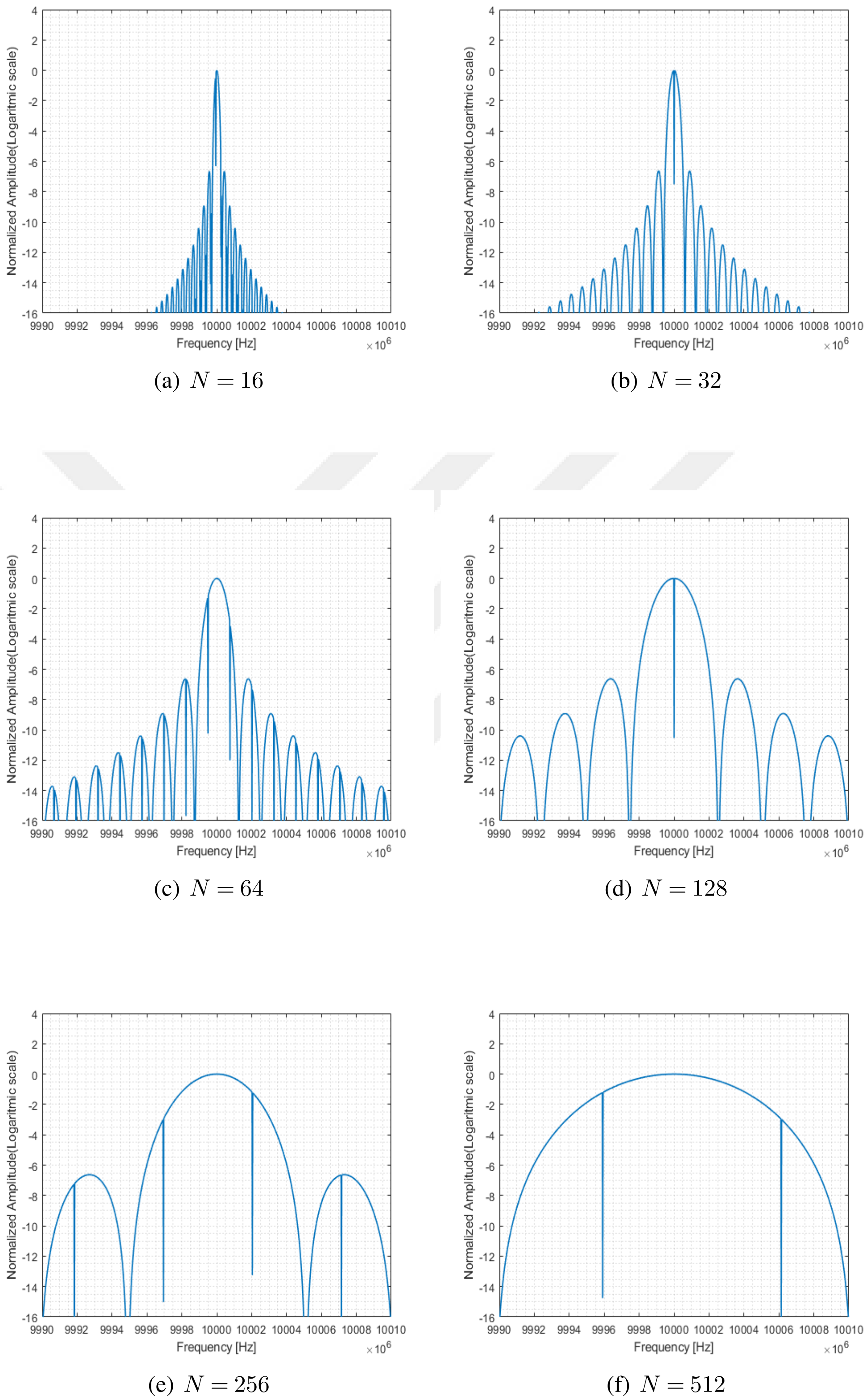

(a) $N = 16$ (b) $N = 32$

(c) $N = 64$ (d) $N = 128$

(e) $N = 256$ (f) $N = 512$

Figure 4.8 : Bandwidth of different numbers of PN code sequences.

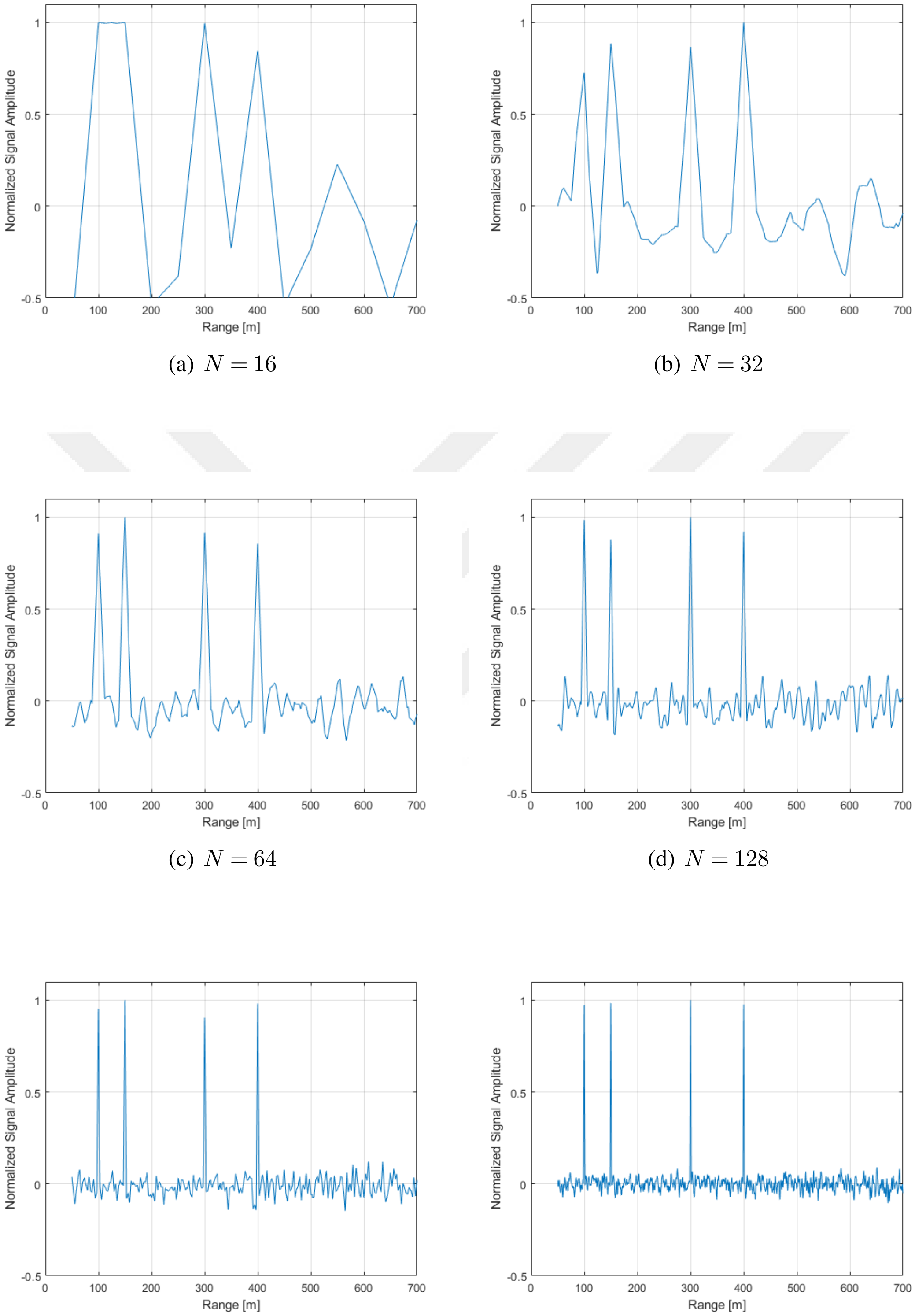

(a) $N = 16$ (b) $N = 32$

(c) $N = 64$ (d) $N = 128$

(e) $N = 256$ (f) $N = 512$

Figure 4.9 : Range profile for different numbers of PN code sequences.

Table 4.3 : The digital phase coded radar bandwidths.

Sequence Length (N)	Bandwidth (MHz)	τ_c (us)
16	0.6	33.4
32	1.24	1.61
64	2.5	0.793
128	5	0.393
256	10.2	0.196
512	20.44	0.097

4.3 Range Profile Extraction with a Realistic Object

In order to better analyze the performance of the PN digital coded radar, a rectangular prism is chosen as the target. The operating parameters of the radar are selected the same as the radar parameters in Table 4.2. The dimensions of the selected rectangular prism, which is the target, are determined as $40m \times 5m \times 5m$. As can be seen in Fig. 4.10, the outer surface of the prism is divided into perpendicular triangles, with each short side $0.5m$.

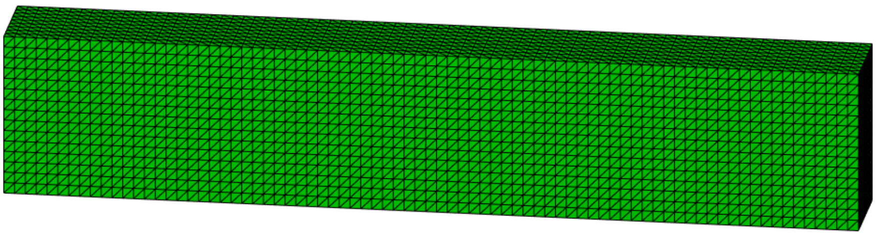

Figure 4.10 : The rectangular prism target model.

A realistic object is modeled by making the RCS calculation of each reflecting point. The RCS calculation of circles with the same area as each small triangle as performed. For the RCS calculation, in (3.4), which is radius of each circle is determined to be $d = 0.19m$, equal to the area of each sub-triangle for the frequency value 10GHz. When the total number of triangles is expressed as M, the receive signal downconverted to the baseband is given as

$$x_{IF}(t) = \sum_{m=1}^{M} \sigma(m) e^{-j2\pi f_c \Delta t_m} \sum_{k=0}^{N-1} a_k g(t - k\tau_{chip} - \Delta t_m). \tag{4.8}$$

The designed radar system is on the drone, as indicated in Fig.4.11, and has been

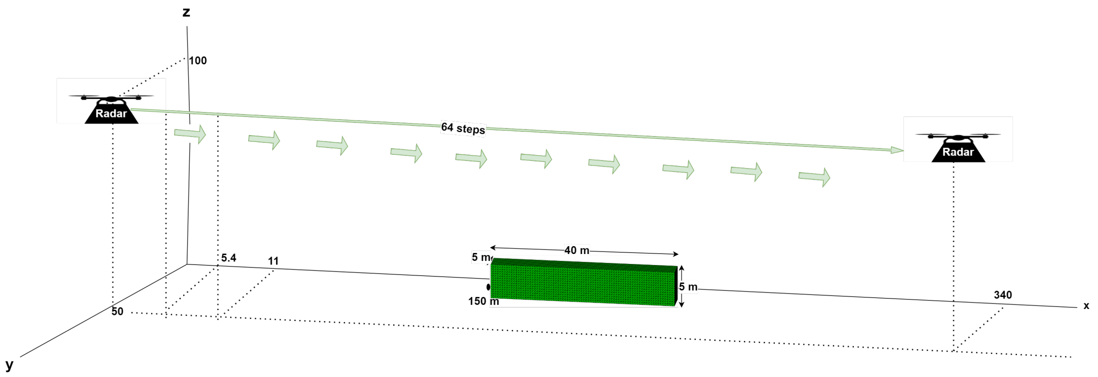

Figure 4.11 : Linear flight profile of the radar system.

determined to move at $100\,m$ altitude, at $50\,m$ on the y-axis, and at 64 equal intervals from $0\,m$ to $340\,m$ according to the x-axis.

For example, a detection process is performed at the first $(0, 50, 100)$ and fiftieth $(200, 50, 100)$ positions of the radar platform in order to extract the dimensions and position of the target object. The amplitude of the extracted range profile is normalized

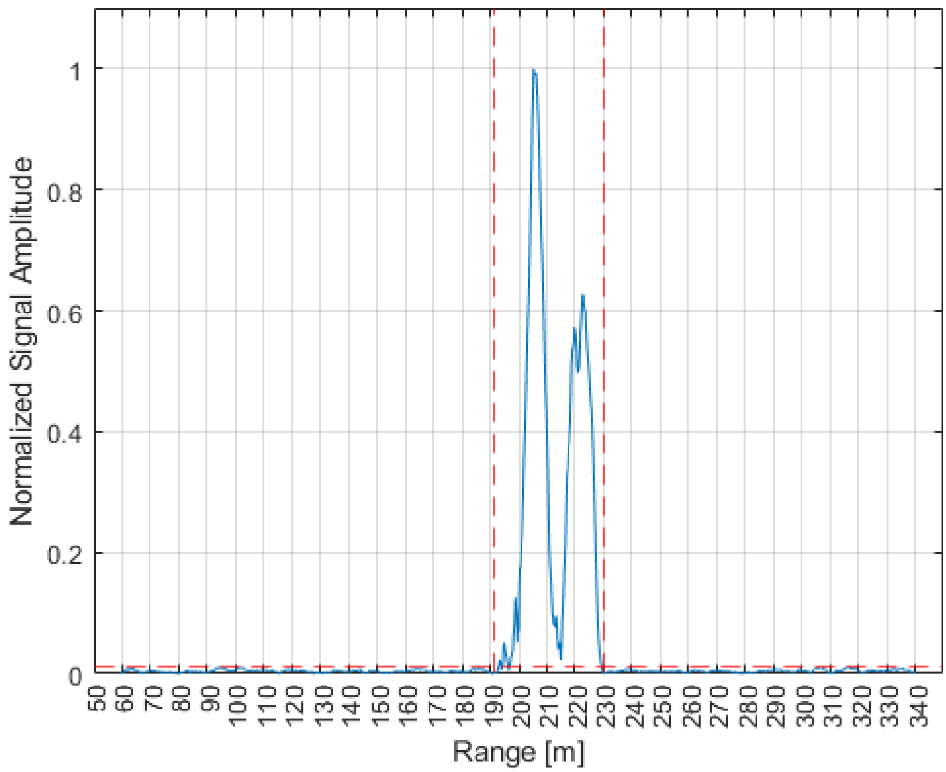

Figure 4.12 : Range profile of rectangular prism in respect to platform 1st position (0,50,100).

and the threshold value is taken as 1% of the maximum peak point. By marking the first and last point where it passes this threshold level, the dimensions of the object are tried to be extracted. As seen in Fig. 4.12, the starting point of the object for the initial

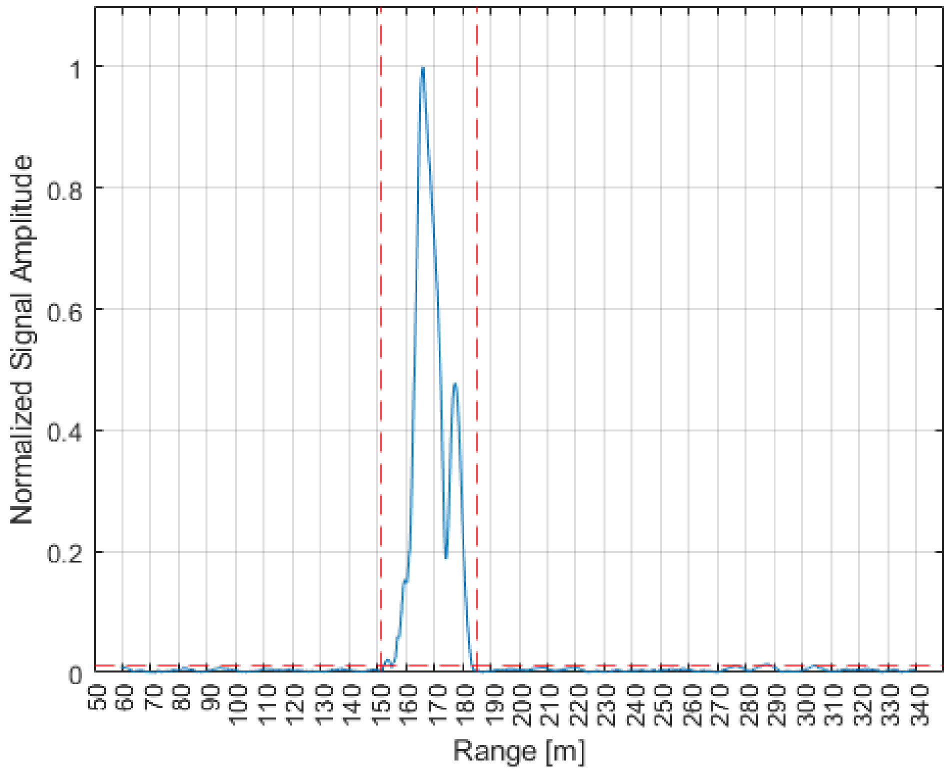

Figure 4.13 : Range profile of rectangular prism in respect to platform 50$^{\text{th}}$ position (264.5,50,100).

position of the radar platform is $190\,m$ and the endpoint is $230\,m$. The radar platform illuminates the object at an angle of about 30 degrees at approximate elevation. The length of the object is around $40\,m$ when looking at the range gates. In the second example, a range profile is drawn for the fiftieth position of the radar. The radar platform is approximately 50 degrees in elevation with the target object. It is relatively closer to the target object than the initial position of the radar. For this reason, as can be seen in Fig. 4.13, the first point of the range gate is displayed as $147\,m$ and the endpoint as $180\,m$. From this point of view, the size of the object is measured as approximately $33\,m$. A synthetic aperture has been created with the linear motion profile of the radar platform so that B-scan image can be generated. The radar does a B-scan with this

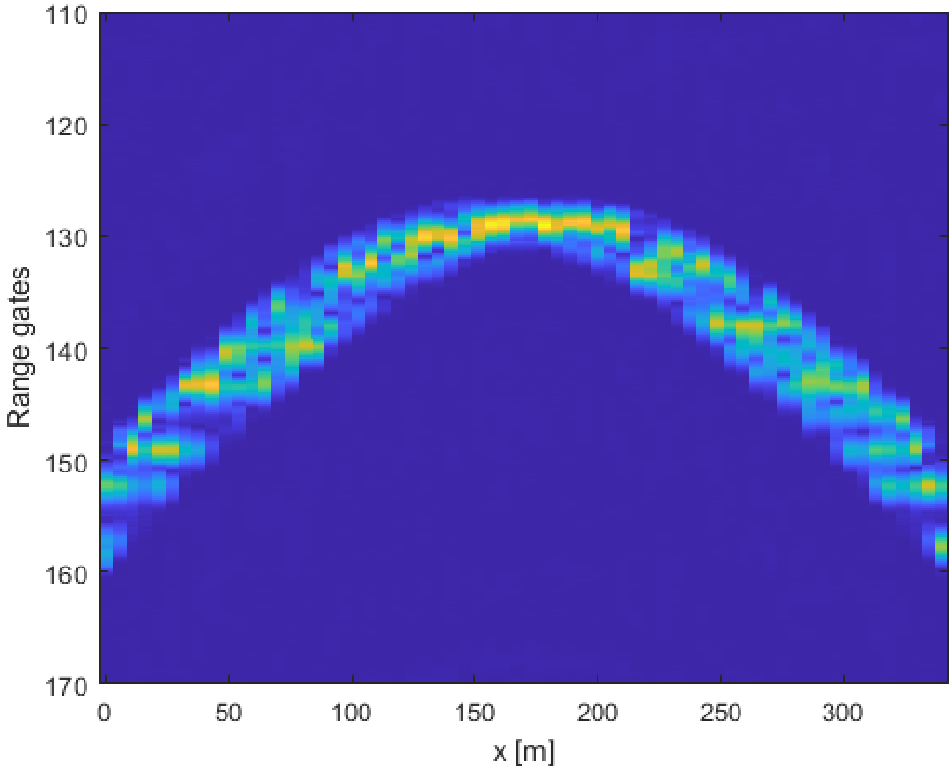

Figure 4.14 : The B-scan of linear flight

linear flight profile. In other words, the radar platform, which makes linear flight, first approached the object and then moved away symmetrically. As it scans in this way, a hyperbola image is formed, as in Fig. 4.14. Since this electromagnetic wave's travel duration between the radar and the illuminated scattering target differ, this object appears as a parabolic hyperbola in the B-scan image. The object's actual position is at the peak of this hyperbola. In order to find the peak point of this hyperbola, the hyperbolic summation method is used [28]. When using the hyperbolic summation algorithm, let's express the vertical depth from the radar to the object with z points and the synthetic aperture along the X axis with x points. In the $\mathbf{R} = \sqrt{z^2 + (\mathbf{X} - x)^2}$, X is the synthetic aperture vector, and R is the route length vector from the antenna to the scatterer. In order to create a 2D image, R is calculated for each x_i and z_i point. In the continuation of the algorithm, the energy of the vector obtained for each range profile is calculated and the generated pixel points are written. As the output of this algorithm, the B-scan image in Fig. 4.15 is obtained. As can be seen, the dimensions of the object

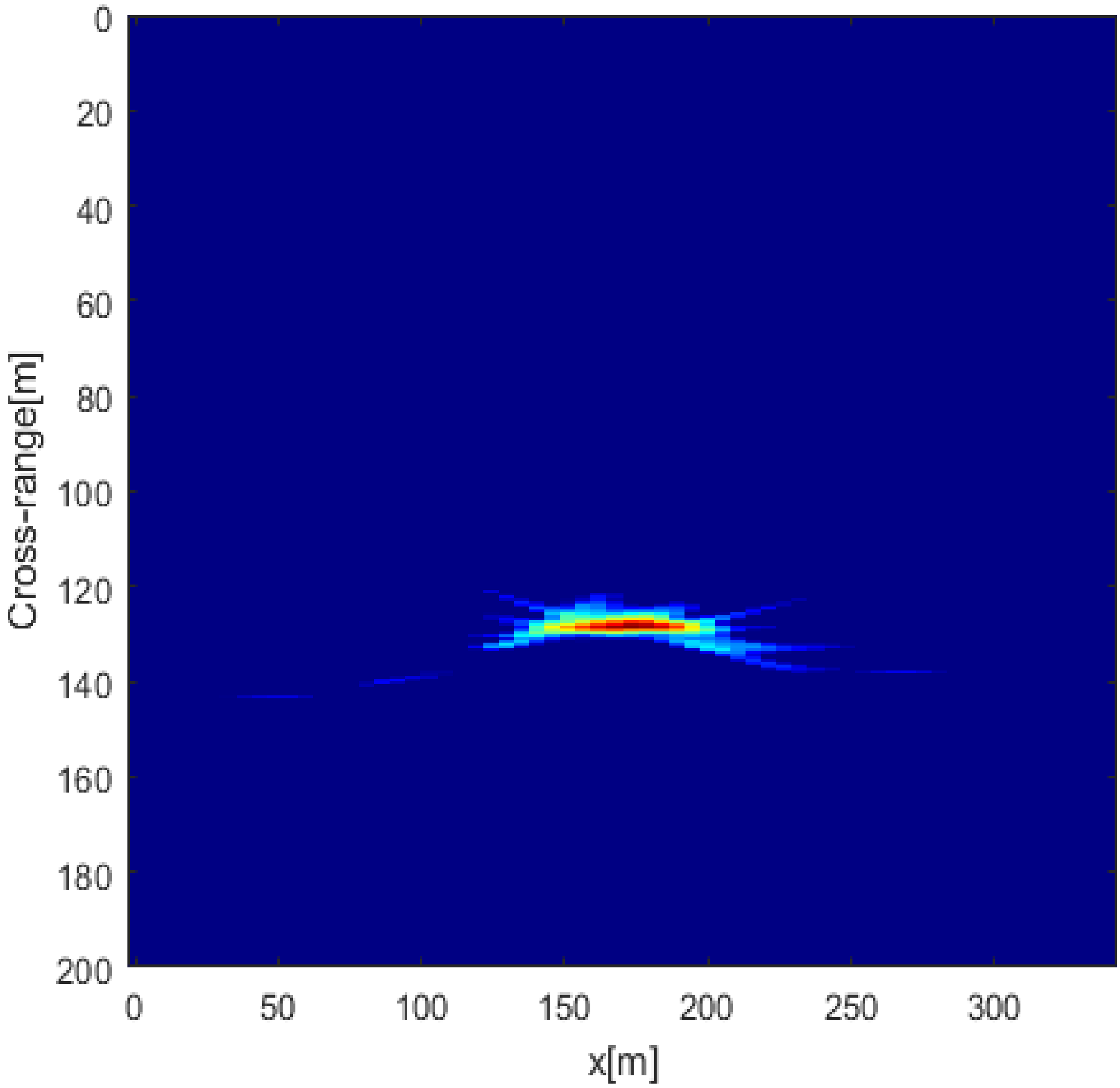

Figure 4.15 : The B-scan image of the rectangular prism.

are 40 meters in length and 5 meters in width in the 2-dimensional image. Two objects are placed as the target of the radar making a linear flight profile. As seen in Fig.4.16, the dimensions of the objects are $20mx5mx10m$, the first of which is placed at 50 meters, and the second object with the same dimensions is placed at 270 meters. The point where the first range profile is drawn is the first position of the radar's flight profile, namely (0,50,100) coordinate. As can be seen in Fig. 4.17, the radar started to see the first object about 125 meters away from itself and informed that it was an object up to 150 meters. The second object extends from 292 meters to 308 meters. When looking at the amplitude values, the object with the parts that radiate closer to the perpendicular angle gets a higher amplitude value. The second range profile is

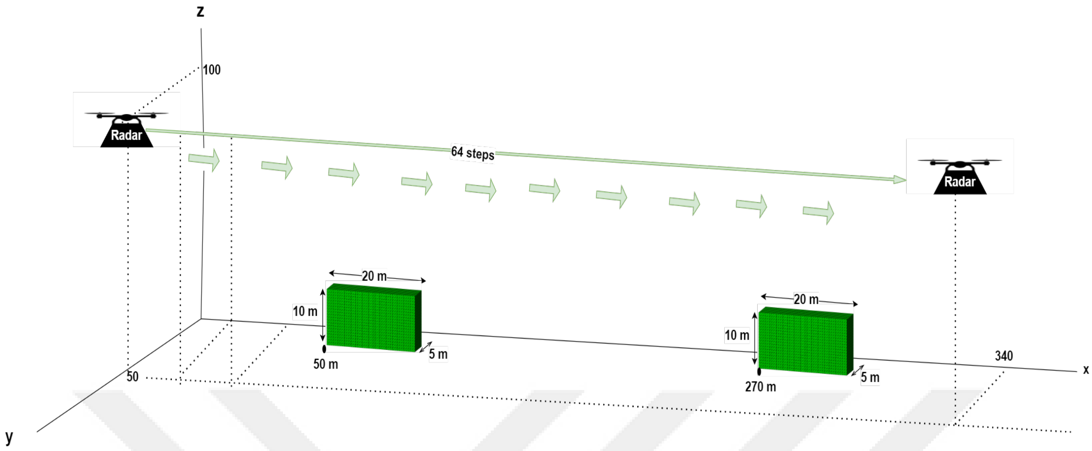

Figure 4.16 : Linear flight profile of the radar system and the two targets.

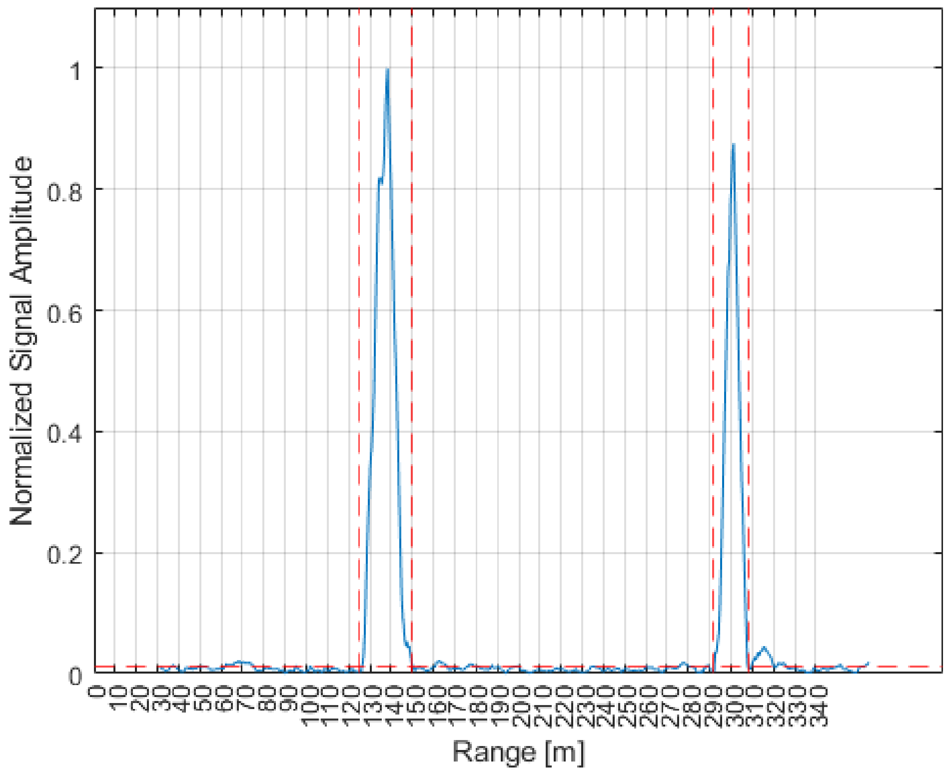

Figure 4.17 : Range profile of two rectangular prisms in respect to platform 1st position (0,50,100).

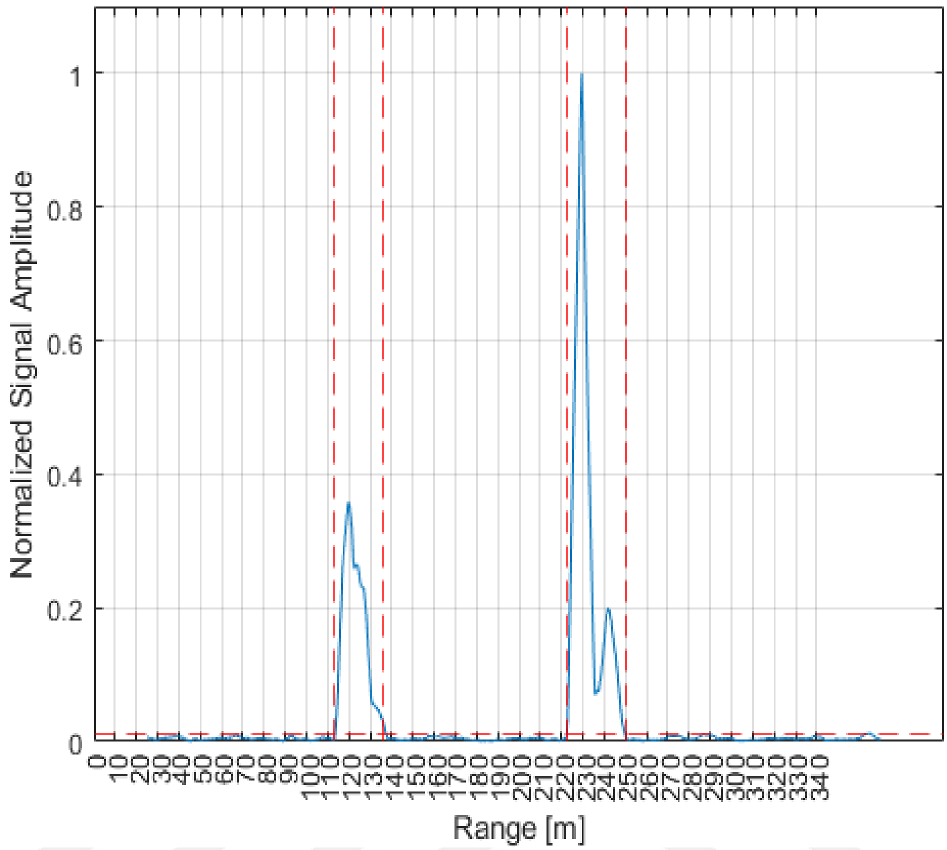

Figure 4.18 : Range profile of two rectangular prisms in respect to platform 50th position (264.5,50,100).

created with the information received from the radar's 50th position (264.5,50,100) coordinates as seen in Fig 4.18. The first object extends from 223 meters to 250. The second object appears closer and higher up and stretches from about 113 meters to 136 meters. The first object has a higher amplitude value because the surface illuminated at right angles has more triangular subparts.

In Fig. 4.19, the B-scan created by the flight profile created for two separate targets is shown. Since the flight is straight flight, two hyperbolic images are formed. The image of the B-scan image obtained by the hyperbolic summation method is given in Fig. 4.20.

While the radar properties remain the same and target object dimensions are $40m \times 5m \times 5m$, a full circle flight profile is created with a radius of $170m$. As can be seen

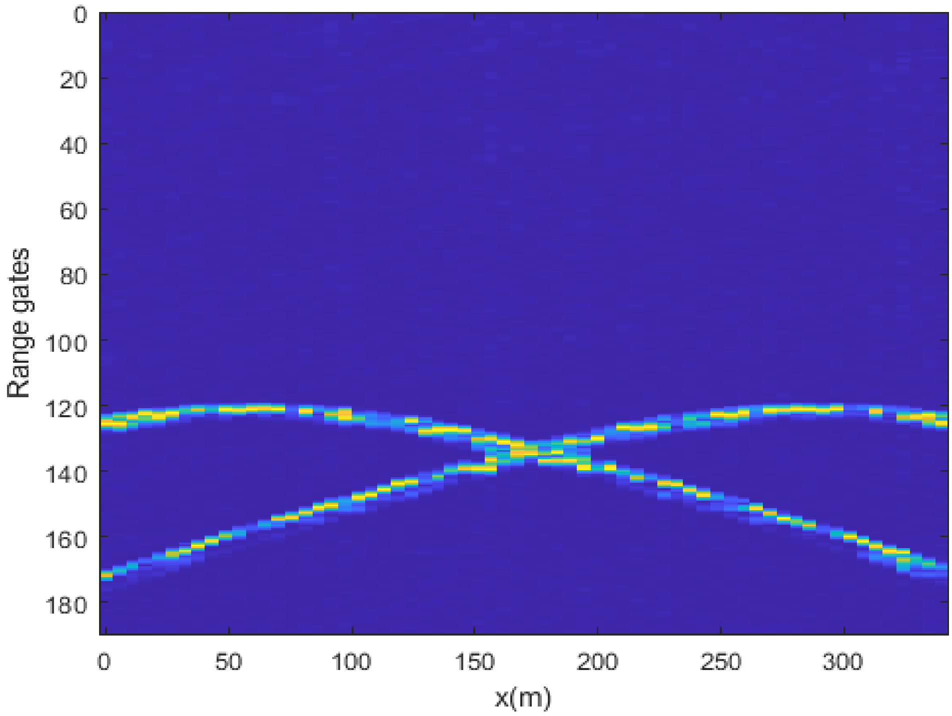

Figure 4.19 : The B-scan of linear flight

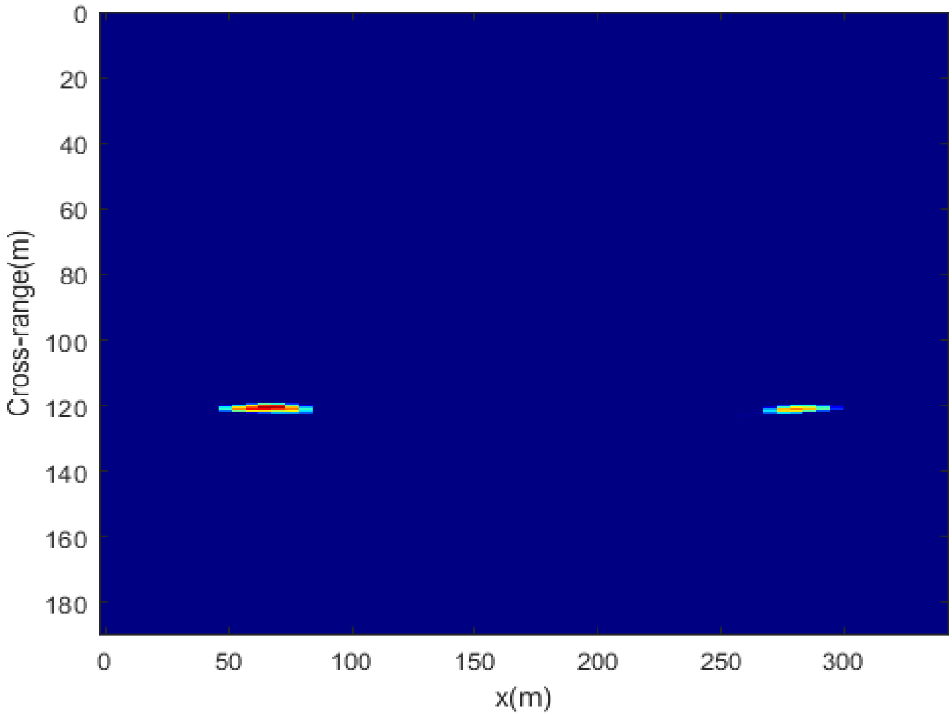

Figure 4.20 : The B-scan image of the two rectangular prisms.

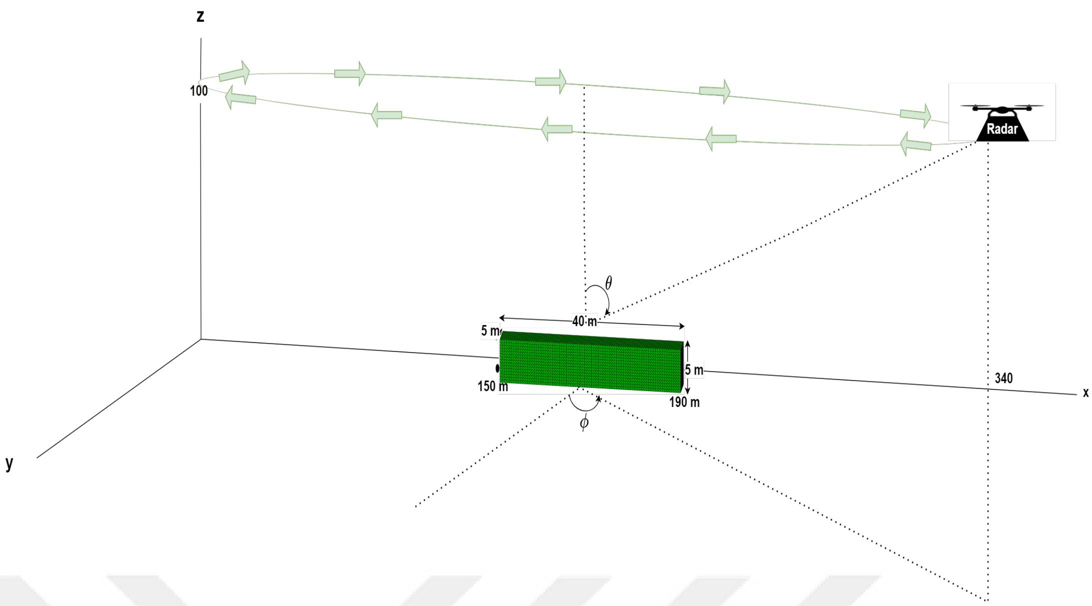

Figure 4.21 : Circular flight profile of the radar system.

in Fig. 4.21, the radar platform moved at 64 different points in a circular flight profile symmetrical with respect to the center of the target object.

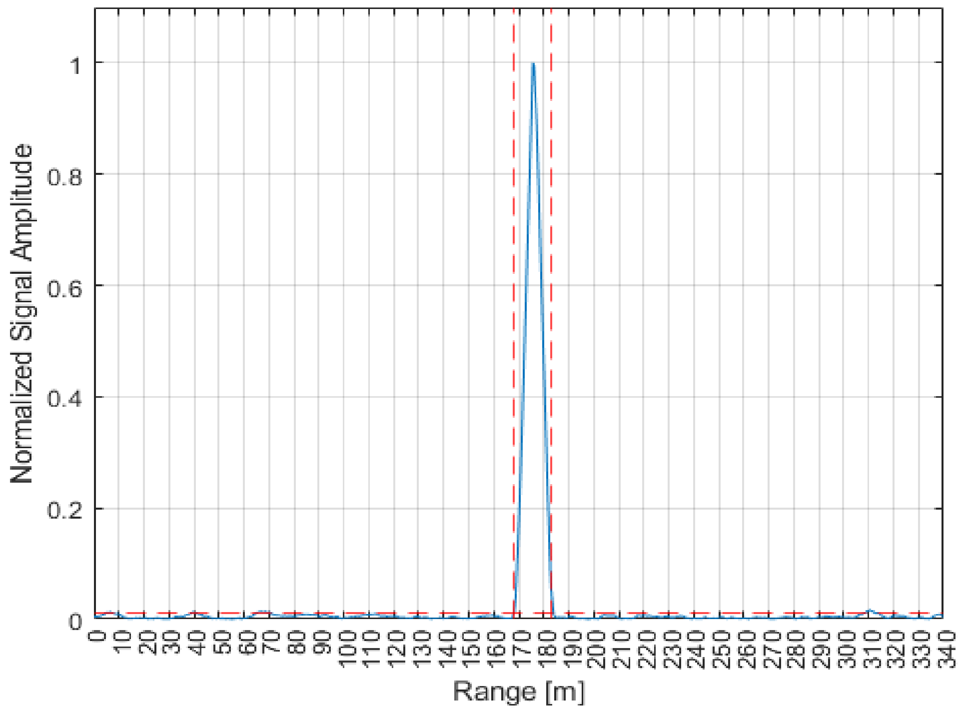

Figure 4.22 : Range profile of rectangular prism in respect to platform in azimuth $\phi = 0°$

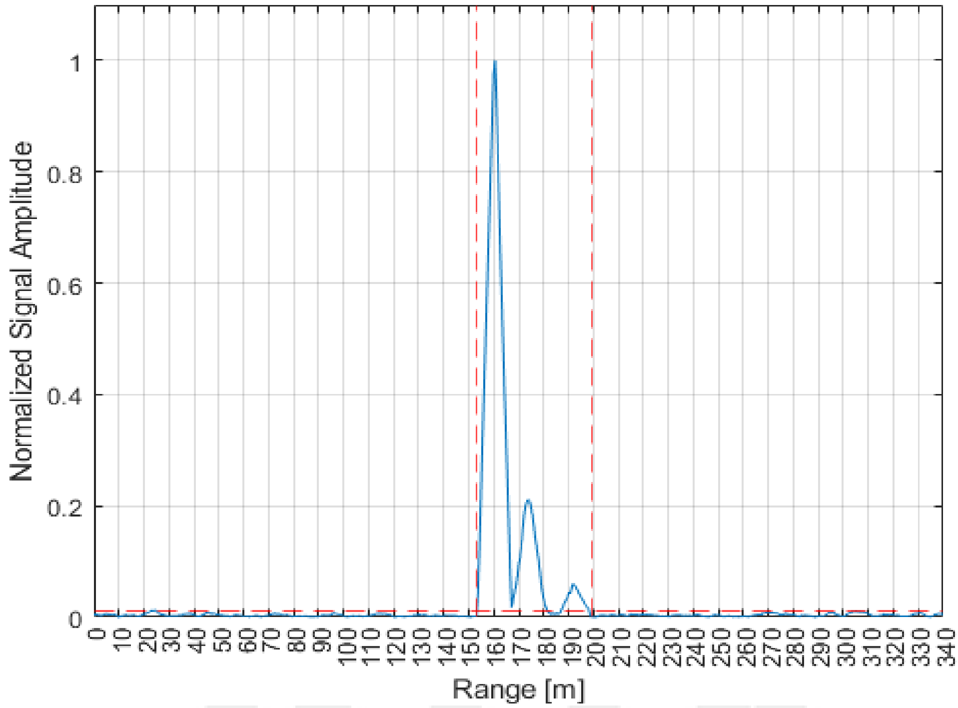

Figure 4.23 : Range profile of rectangular prism in respect to platform in azimuth $\phi = 90°$.

The range profile obtained when the radar platform azimuth angle is $0°$ is given in Fig.4.22. The first starting point of the range gate is $169\,m$ and the ending point appears to be approximately $181\,m$.The area where the object is located has been calculated as approximately $12\,m$. Since it has a height of $100\,m$ in the z-axis, it is predicted that this value is obtained by reflections from other surfaces. When the azimuth angle of the radar to the target is approximately 90 degrees, the range profile created is given in Fig. 4.23.

As can be seen, the starting point of the range gate is $150\,m$ and the ending point is $190\,m$. Since the object has a long side of $40\,m$, a realistic range profile is obtained. The reason why the range profile produced by the 90 degree angle that sees the long side achieves a more accurate result compared to 0 degree is that the resolution is lower because there are fewer triangle points on the short side.

In order to compare the results obtained from different points in the extracted range profiles, their normalized forms with each other are given in Fig. 4.24. As seen in Fig.

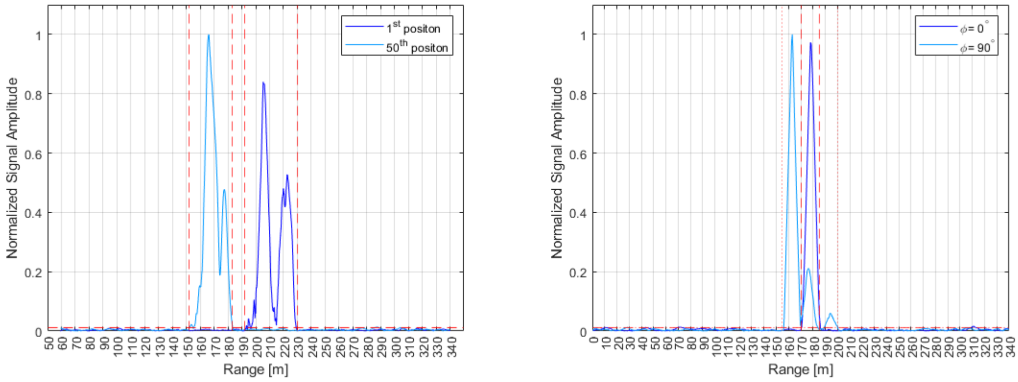

(a) Linear flight range profile (b) Circular flight range profile

Figure 4.24 : Range profiles normalized to each other for two flight profiles.

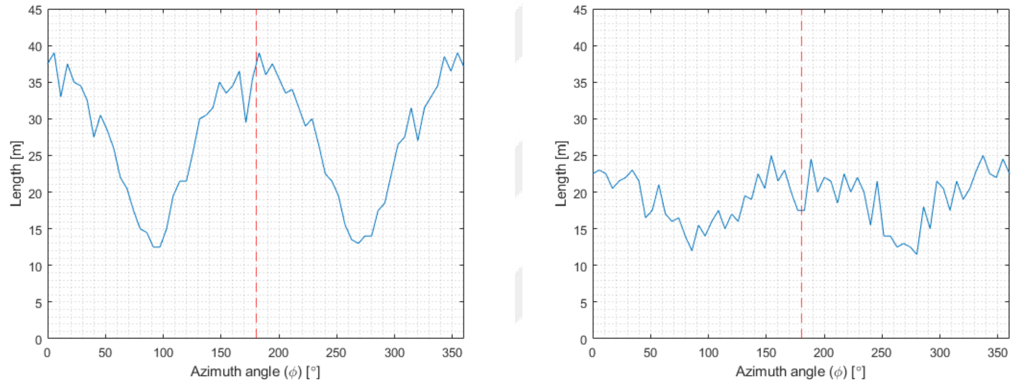

(a) The prism dimensions are $40x5x5\,m$ (b) The prism dimensions are $20x10x5\,m$

Figure 4.25 : Width and length of two different rectangular prisms on full azimuth angle.

4.24(a), the reflection is more in the 50th position, which is close to the target object and illuminates more area. Likewise, the amplitude value, which appears at 90 degrees in azimuth angle in Fig. 4.24(b), is higher.

In order to see the symmetry of the range profiles in 360 degrees coverage in azimuth, calculations are made for two different prisms. The dimensions of the first object are chosen to be $40x5x5\,m$ and the dimensions of the second object to be $20x10x5\,m$. It is seen in Fig. 4.25(a) and Fig. 4.25(b) that the radar platform covers 360 degrees in azimuth and the measurements taken from 64 different points are 180 degrees symmetrical when the distances of the range gates are subtracted.

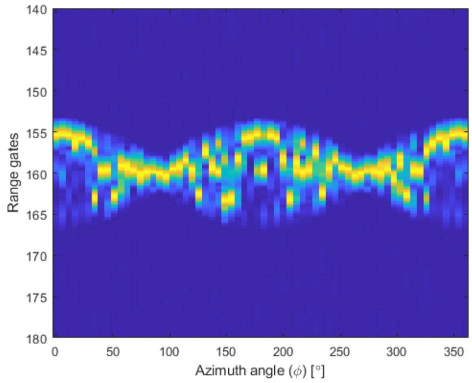

(a) The B-scan of a prism with dimensions of $40x5x5\,m$

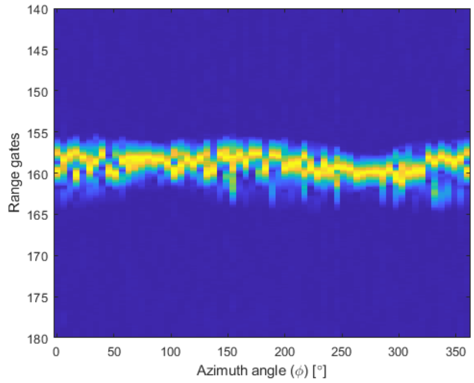

(b) The B-scan of of a prism with dimensions of $20x10x5\,m$

Figure 4.26 : The B-scan of two different targets.

If the range profiles of two different sized prisms at 64 different points are turned into an image, it is as in Fig. 4.26. While a longer and narrower object is observed in the image in Fig. 4.26(a), it is observed that it is shorter and wider in Fig. 4.26(b). The inference made here is important in terms of seeing the comparison of the target objects with each other.

5. CONCLUSION

In this thesis study, firstly, it started by giving information about the working mechanisms and general characteristics of radars. Then, the increase in the use of noise radars with the developing technology was mentioned and information was given about the noise radars and their usage areas. The beacon structure of noise radars is examined, and the steps and processes required for target detection are discussed. With the developing technology, the use of digital radars has increased. In this way, it is not very difficult to design digital radars with the help of faster sampling ADCs. Inspired by the increase in the use of noise radars and digital code radars, in this study, which uses pseudo-noise coded radar structures, phase coding sequences that are frequently used in classical phase coded radars are explained. Among these code sequences, Barker codes, Frank codes, P1, P2, and Px, Zadoff–Chu code and Pseudo-Noise code series are explained. How these sequences are formed in numeric blocks is examined and their cross-correlation properties are compared.

In the following, system models of noise radars are explained. The receiver and sender blocks of the radar system are detailed and the RF blocks used are introduced. Thus, the transmitting and receiving mechanism of the radar system has been introduced in detail. At the same time, information was given about the radar platform used. The radar system, which is designed as a drone payload, is explained from which angles it can look at the target and how it can fly. First, point scatterers were used for the target, and then a rectangular prism-shaped target was simulated to be realistic. The target object, the rectangular prism, was divided into small triangles and the radar cross-sectional area of each was calculated. Physics optics methods were used while calculating this radar cross-sectional area. The calculations are explained in detail and the result of the change of the radar platform according to the angle it makes with the triangular pieces forming the target object is given.

A pseudo-noise array was created in the MATLAB environment and this array was used as the phase code of the radar. Bandwidths of radar transmit signals generated by changing the length of the array are shown. It has been shown that as the length of the code sequence is increased, the bandwidths increase, thus increasing the detection capability of the radar. In the first stage of the simulation, 4 point scatterers are placed in certain regions in space. Gaussian noise is added to the echo signal returning from the radar. The locations of 4 point scatterers were determined in the extracted range profile. Successfully demonstrated results. Afterward, the radar on the drone made a linear flight from 0 meters to 340 meters on the target model measuring 40 m x 5 m x 5 m and took measurements at 64 different points. A matrix was created with the data collected in the transmit signal, which was created using a 1024-length pseudo noise code. As an example, the range profile is obtained by using the correlation method of the signal received from the first and fiftieth position. The information that the width of the target is 40 meters has been removed from this profile. In this way, it has been observed that the size information of the objects can be obtained from this radar system. The visual created from the range profiles of the signals received from 64 different locations has been added to this study. Due to the linear flight of the radar, a movement towards and away from the target is provided. For this reason, the image of the range profiles is hyperbolic. Hyperbolic summation method was used to get the image of the target and its exact location is shown in the image. The second radar flight was circular. Radar echoes were collected from 64 points simulated flight, forming a circle with a diameter of 170 meters, with the target at the center point. Radar range profiles are now flat, not hyperbolic. This is because the radar is at the same distance from the target at every point. At the same time, it has been shown that the extracted lengths of the target are symmetrical as a result of this movement. Düzelt!!!!!!!!!!!!

As a result, the range and dimensions of the target can be accurately deduced and the phase coded radar has been shown to be successful. In future studies, radar performance can be tested by changing the target or using a real model.

REFERENCES

[1] **Savci, K.**, **Stove, A.G.**, **De Palo, F.**, **Erdogan, A.Y.**, **Galati, G.**, **Lukin, K.A.**, **Lukin, S.**, **Marques, P.**, **Pavan, G. and Wasserzier, C.** (2020). Noise radar—overview and recent developments, *IEEE Aerospace and Electronic Systems Magazine*, *35*(9), 8–20.

[2] **Malanowski, M. and Kulpa, K.** (2011). Target Detection in Continuous-Wave Noise Radar in the Presence of Impulsive Noise., *Acta Physica Polonica, A.*, *119*(4).

[3] **Savci, K.**, **Stove, A.G.**, **Erdogan, A.Y.**, **Galati, G.**, **Lukin, K.A.**, **Pavan, G. and Wasserzier, C.** (2019). Trials of a noise-modulated radar demonstrator–first results in a marine environment, *2019 20th International Radar Symposium (IRS)*, IEEE, pp.1–9.

[4] **Kulpa, K.** (2013). *Signal processing in noise waveform radar*, Artech House.

[5] **Skolnik, M.I.** (1962). Introduction to radar, *Radar handbook*, *2*, 21.

[6] **Horton, B.** (1959). Noise-modulated distance measuring systems, *Proceedings of the IRE*, *47*(5), 821–828.

[7] **Narayanan, R.M.**, **Xu, Y.**, **Hoffmeyer, P.D. and Curtis, J.O.** (1998). Design, performance, and applications of a coherent ultra-wideband random noise radar, *Optical Engineering*, *37*(6), 1855–1869.

[8] **Narayanan, R.M. and Dawood, M.** (2000). Doppler estimation using a coherent ultrawide-band random noise radar, *IEEE Transactions on Antennas and Propagation*, *48*(6), 868–878.

[9] **Xu, X. and Narayanan, R.M.** (2001). Range sidelobe suppression technique for coherent ultra wide-band random noise radar imaging, *IEEE Transactions on Antennas and Propagation*, *49*(12), 1836–1842.

[10] **Tarchi, D.**, **Lukin, K.**, **Fortuny-Guasch, J.**, **Mogyla, A.**, **Vyplavin, P. and Sieber, A.** (2010). SAR imaging with noise radar, *IEEE Transactions on Aerospace and Electronic systems*, *46*(3), 1214–1225.

[11] **Lukin, K.**, **Stove, A.**, **Kulpa, K.**, **Calugi, D.**, **Palamarchuk, V. and Vyplavin, P.** (2013). Kaband groundbased noise SAR trials in various conditions, , (12,№ 1), 145–151.

[12] **Thayaparan, T. and Wernik, C.** (2006). Noise radar technology basics, **Technical Report**, DEFENCE RESEARCH AND DEVELOPMENT CANADA OTTAWA (ONTARIO).

[13] **Muralidhara, N.**, **Rajesh, B.**, **Biradar, R.C. and Jayaramaiah, G.** (2017). Designing polyphase code for digital pulse compression for surveillance radar, *2017 2nd International Conference on Computing and Communications Technologies (ICCCT)*, IEEE, pp.1–5.

[14] **Mahafza, B.R.** (2005). *Radar systems analysis and design using MATLAB*, Chapman and Hall/CRC.

[15] **De Maio, A. and Farina, A.** (2009). New trends in coded waveform design for radar applications, **Technical Report**, UNIVERSITA DI NAPOLI FEDERICO II (ITALY) DIPARTIMENTO DI INGEGNERIA ....

[16] **Richards, M.A.**, **Scheer, J.**, **Holm, W.A. and Melvin, W.L.** (2010). Principles of modern radar.

[17] **Levanon, N.** (1988). Radar principles, *New York*.

[18] **Shubhaker, B.** (2017). Phase Coded Radar Signals - Frank Code & P4 Codes, *International Journal of Advance Research*, *3*(6).

[19] **Jamil, M.**, **Zepernick, H.J. and Pettersson, M.I.** (2008). Performance assessment of polyphase pulse compression codes, *2008 IEEE 10th International Symposium on Spread Spectrum Techniques and Applications*, IEEE, pp.166–172.

[20] **Lewis, B. and Kretschmer, F.** (1981). A new class of polyphase pulse compression codes and techniques, *IEEE Transactions on Aerospace and Electronic Systems*, (3), 364–372.

[21] **Chu, D.** (1972). Polyphase codes with good periodic correlation properties (corresp.), *IEEE Transactions on information theory*, *18*(4), 531–532.

[22] **Haykin, S.** (2008). *Communication systems*, John Wiley & Sons.

[23] **Brückner, S.** (2016). *Maximum length sequences for radar and synchronization*, Cuvillier Verlag.

[24] **Rouphael, T.J.** (2008). *RF and Digital SIGNAL processing for Software-defined radio*, Elsevier.

[25] **Shirude, N.**, **Pinto, R. and Panse, M.** Design and Simulation of RADAR Transmitter and Receiver using Direct Sequence Spread Spectrum in MATLAB Simulink.

[26] **Meyers, D.** (2012). *Radar Target Detection: Handbook of Theory and Practice*, Elsevier.

[27] **Jenn, D.** (2005). *Radar and laser cross section engineering*, American Institute of Aeronautics and Astronautics, Inc.

[28] **Özdemir, C.**, **Demirci, Ş.**, **Yiğit, E. and Yilmaz, B.** (2014). A review on migration methods in B-scan ground penetrating radar imaging, *Mathematical Problems in Engineering*, *2014*.

CURRICULUM VITAE

Name Surname: Şevval Karabağ Çaha

EDUCATION:

- **B.Sc.:** 2014-2019, İstanbul Technical University, Faculty of Electrical and Electronics Engineering, Department of Electronics and Communication Engineering
- **B.Sc.:** 2014-2020, İstanbul Technical University, Faculty of Electrical and Electronics Engineering, Department of Control and Automation Engineering

PROFESSIONAL EXPERIENCE AND REWARDS:

- 2021- Electronic Warfare Systems Engineer, ASELSAN A.Ş., Ankara, Turkey
- 2019- 2021 Research Assistant, Istanbul Technical University, Istanbul, Turkey

PUBLICATIONS, PRESENTATIONS AND PATENTS ON THE THESIS:

- Karabağ, Ş., Ferhanoğlu, O., Özdemir, Ö. (2020, October). Conformal Antenna for Capsule Endoscopy. In 2020 28th Signal Processing and Communications Applications Conference (SIU) (pp. 1-4). IEEE.